

# Association of two semiflexible polyelectrolytes by interchain linkers: Theory and simulations

Itamar Borukhov

*Department of Chemistry and Biochemistry, Department of Physics, University of California at Los Angeles, Los Angeles, California 90095*

Kun-Chun Lee

*Department of Chemistry and Biochemistry, University of California at Los Angeles, Los Angeles, California 90095*

Robijn F. Bruinsma

*Department of Physics, University of California at Los Angeles, Los Angeles, California 90095*

William M. Gelbart and Andrea J. Liu

*Department of Chemistry and Biochemistry, University of California at Los Angeles, Los Angeles, California 90095*

Mark J. Stevens

*Sandia National Laboratories, P.O. Box 5800, MS 0316, Albuquerque, New Mexico 87185*

(Received 14 December 2001; accepted 4 April 2002)

The aggregation of two highly charged semiflexible polyelectrolytes in the presence of generalized linkers is studied theoretically. This model provides insight into biological processes such as DNA condensation and F-actin self-assembly induced by either multivalent counterions or bundling proteins. The interplay between the bending rigidity of the chains and their electrostatic interactions leads to an effective interlinker interaction that is repulsive at large distances and attractive at short ones. We find a rounded phase transition from a dilute linker gas where the chains form large loops to a dense disordered linker fluid where the chains are almost parallel. The onset of chain pairing occurs as soon as the free energy of a pair of chains becomes lower than that of two isolated chains and is located well within the crossover regime between the two linker phases. Our main findings are confirmed by molecular dynamics simulations of two semiflexible charged chains in a mixture of monovalent and polyvalent counterions. This simple model allows us to recover qualitative features of experimental aggregation diagrams of DNA and F-actin and can also be used to study DNA denaturation. © 2002 American Institute of Physics. [DOI: 10.1063/1.1481382]

## I. INTRODUCTION

Biomolecules, notably nucleic acids and proteins, are invariably charged because of their need to be soluble over a broad range of concentrations in aqueous solution. Furthermore, their charge provides a powerful yet subtle basis for control of their aggregation and condensation, both with themselves and each other. Of particular importance is the condensation of DNA in the presence of multivalent counterions.<sup>1–4</sup> *In vitro* studies of highly dilute DNA solutions have established that DNA can be condensed in this way into hexagonally-packed, circumferentially-wound, toroids whose interaxial spacings are as small as those in crystalline DNA. *In vivo* analogies of these structures have been studied most thoroughly in bacterial viral capsids, where the high density of DNA is necessary for storage purposes. Indeed, the genes carried by the condensed viral genome are not accessible for transcription or replication until the DNA is “freed” by injection into the bacterial cell.

Polymerized actin (F-actin), a ubiquitous and important structural protein, is comparably strongly condensed by the addition of either multivalent counterions or “bundling” (“linker”) proteins.<sup>5–9</sup> Because the actin filaments are stiff,

i.e., not long compared to their persistence lengths, their condensates consist in general of straight bundles of close-packed filaments. Synthetic stiff polyelectrolytes such as poly(*p*-phenylene benzobisthiazole) (PBZT) can also be induced to form bundles.<sup>10</sup> In all the above cases, when the concentration of condensing agents is not sufficiently high, it is expected that some sort of intermediate structure will arise, involving a network of junctions at which individual or small numbers of counterions or linker proteins are shared between pairs of polyelectrolyte molecules.<sup>11</sup>

The effect of multivalent counterions on the interaction between highly-charged polyelectrolytes has been the focus of a great deal of attention in the past decade, both experimentally<sup>13</sup> and theoretically.<sup>14–23</sup> Of special interest is the attractive force that can arise between such chains, which necessarily implies the qualitative breakdown of the mean-field (Poisson–Boltzmann) theory of electrostatic interactions. Two main mechanisms have been proposed for the origin of this attraction. In both mechanisms, the condensed counterions in a narrow layer surrounding the chains give rise to charge distributions that are highly correlated along the axes of the chains; the attraction arises from anticorrelations between these charge distributions. At low

temperatures/high fixed-charge densities the attraction is due to short-ranged correlations in the charge distributions, reminiscent of a Wigner crystal;<sup>18,20–22,24–26</sup> at high temperatures/low fixed-charge densities, on the other other hand, the attraction is due to long-wavelength fluctuations in the charge distributions.<sup>14,17,19,26,27</sup> An additional contribution to the attraction arises from the nonisotropic distribution of counterions in the plane perpendicular the chain axes.<sup>15,23</sup>

In this standard view of aggregation of highly-charged chains, one focuses on how multivalent counterions mediate attractive effective interactions between the chains. By contrast, in this paper we take the opposite view—we consider how the chains mediate effective interactions between the multivalent ions.<sup>28,29</sup> We then consider the consequences of these effective interactions on chain aggregation. Indeed, we sidestep the question of the origin of the attraction by treating the multivalent counterions *explicitly* as interchain linkers, i.e., particles that hold the two chains together by a short-ranged attraction. By keeping the discrete nature of the multivalent counterions instead of replacing them with a continuous distribution surrounding the chains we manage to keep the most important effect of ion correlations. On the other hand, since the correlations between monovalent ions are not expected to play an important role, we treat them as a continuous background, which leads to the standard exponential screening of electrostatic interactions. It should thus be emphasized that, in our approach, multivalent counterions are treated qualitatively differently from monovalent ones.

One advantage of treating the multivalent counterions as linkers is that our approach can be generalized to include other forms of linkers, as well. In particular, we consider how chains mediate effective interactions between binding proteins that connect the chains together. Thus, we treat both multivalent counterions and bundling proteins as generalized linkers that adsorb onto the polyelectrolytes and result in the formation of interchain junctions. To gain insight into the phenomenon of chain aggregation, we focus on a simplified system, namely a pair of semiflexible polyelectrolytes in the presence of generalized linkers. We note that a strong similarity can be seen between the theory treated here and that of DNA melting,<sup>30–35</sup> where a double-stranded DNA molecule denatures—separates—into two single-stranded chains. In this latter case the role of linkers is played by the hydrogen bonds connecting complementary base pairs.

We begin with an analytical theory. First (Sec. II) an effective interaction between linkers is derived, which takes into account both the elastic (bending) energy of the individual chains and the interchain electrostatic repulsions. This interaction is found to be nonmonotonic. At short distances, there is an effective attraction between linkers whose strength varies quadratically with the charge density of the chains; this attraction is cut off at still shorter distances by the direct repulsion (electrostatic and hard core in origin) between linkers. At larger distances there is an effective repulsion mediated by the bending energy of the chains. In Sec. III we derive the statistical thermodynamic properties of a system of particles (the linkers) interacting through an effective potential of this kind. The system is essentially one-dimensional (1D), with only nearest-neighbor interactions;

accordingly, no true, first-order, phase transition is found. Nevertheless, upon increase in the chemical potential of linker we observe a dramatic crossover (“rounded phase transition”) from a dilute to a condensed state of this 1D system of interacting particles. By analyzing the typical chain configurations accompanying each thermodynamic state we are able to conclude that the dilute phase corresponds to the chains forming large loops (with sizes exceeding the chain persistence length) separated by isolated linkers, while the condensed state is associated with essentially parallel chains that share a high density of linkers. While the slope of linker density vs chemical potential is finite, it is large enough to identify a distinct region in which low and high density fluids coexist at essentially constant chemical potential. The position of this region is determined by the relative magnitudes of intrachain bending energy and interchain electrostatic repulsion. Further, it always contains the density at which the free energy of a pair of chains becomes lower than that of two isolated chains. We predict accordingly that when chains first begin to associate (pair) in the presence of linkers (multivalent counterions or bundling proteins) they do so along only part of their length and that the density of shared linkers is constant as further linker is added.

The above picture is borne out nicely in a series of molecular dynamics simulations that elucidate this process. The simulations are described in Sec. IV, where we treat a pair of semiflexible charged chains in the presence of neutralizing counterions. The counterion fluid is composed of a mixture of monovalent and trivalent counterions. The simulations are aimed at determining the stability of two-chain complexes for different counterion mixtures, varying between purely monovalent and (almost) purely trivalent. We found that below a certain threshold number of trivalent counterions  $N_{z=3} = N^*$  the chains do not hold together and separate from each other. Above it, the chains remain paired in a very special way; along some fraction,  $f_2$ , of their total length they are essentially parallel and share some of the trivalent counterions serving as interchain linkers. Upon further increase in  $N_{z=3}$ ,  $f_2$  increases (linearly with  $N_{z=3}$ ) up to its maximum value (unity) at  $N^{**}$ . Throughout this regime ( $N^* \leq N_{z=3} \leq N^{**}$ ) the density of linkers remains constant, corresponding to the condensed state predicted by our theory, and consistent with the specific prediction that the onset of pair stability occurs within the two-phase coexistence region, i.e., as soon as chains are paired they are in a parallel configuration with a high-density of linkers. Above  $N^{**}$  further addition of multivalent counterions leads to an increase in the density of linkers and to a saturation of the strength of binding (pair association).

## II. THE LINKERS AND THEIR INTERACTIONS

### A. Introduction

As discussed in Sec. I, our aim in this section is to construct an effective pair potential for linkers, including the effects of chains, which we will then use in Sec. III to solve for the phase behavior of the system.

We start with a description of the full system and reduce

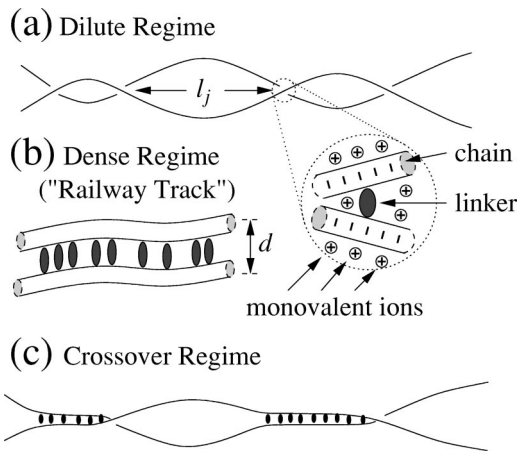


FIG. 1. Schematic view of two chains connected by linkers at (a) low linker densities (the dilute regime); (b) high densities (the disordered “railway track” structure); and (c) intermediate densities (the crossover regime).

the problem to an effective linker–linker interaction in the following subsections. Linkers are treated explicitly while monovalent salt ions are included only as a screening background leading to a Debye–Hückel electrostatic interaction of the form,

$$V(r) = \frac{l_B}{r} e^{-\kappa r} \quad (1)$$

between charges on different chains.<sup>36</sup> In the above equation and in the following discussion all energies are expressed in terms of the thermal energy  $k_B T$ . The screening length  $\kappa^{-1}$  is related to the salt concentration  $c_s$  through  $\kappa^2 = 8\pi l_B c_s$ , the Bjerrum length  $l_B = e^2/\epsilon k_B T$  being the length scale on which the interaction between two monovalent ions is equal to the thermal energy—it is about 7 Å for an aqueous solution (dielectric constant  $\epsilon \approx 80$ ) at room temperature. The important feature of this approach is that correlations between the multivalent counterions are taken into account while those of the salt ions are neglected. We believe that this simplified picture maintains the essential characteristics of the system and allows us to obtain important insight regarding the bundling process.

A schematic view of a multivalent ion forming a linker is presented in Fig. 1. It gains electrostatic energy if it is shared by two charged chains. A reliable estimate of this energy gain (denoted  $2\epsilon_0$ ) depends on many factors including the number of monovalent and multivalent ions in the solution, the radii of the chains and the exact structure of the ionic layer surrounding the two chains. In the case of linker proteins the energy gain is due to specific interaction between the binding sites of the protein and the long chains. It will be treated here as a phenomenological quantity. The distance between the axes of the two chains at the linkage point (center to center) is  $d \approx 2r_s + b$ , where  $r_s$  is the chain radius and  $b$  is the linker diameter. Possible variations in the length of the link are neglected in this model.

The presence of a linker forces two negatively charged chains to remain within a small distance of one another. Due to their strong electrostatic repulsion, the lowest energy configuration is obtained when the two chains are perpendicular

to each other. More specifically, the angular dependence of the electrostatic energy of two straight chains is<sup>43</sup>

$$E_{\text{el}} = \frac{2\pi\xi^2 e^{-\kappa d}}{\kappa l_B \sin\theta} \equiv \frac{\Gamma}{\sin\theta}, \quad (2)$$

where  $\xi = l_B/l_q$  is the effective Manning–Oosawa parameter of the charged chains.<sup>14,44</sup> The line charge density of the chains is negative and equal to  $-e/l_q$ , where  $l_q$  is the average charge separation along the chain. We will see below that  $\Gamma$  is an important energy scale of the system.

The effective interaction between linkers is governed by the interplay between chain bending rigidity and repulsive interchain electrostatic interactions. Clearly, the chain bending rigidity favors parallel alignment of straight chains. On the other hand, the electrostatic repulsion between chains favors a large crossing angle between the two chains at each junction; this interaction therefore results in a torque that tends to bend the two chains.

In setting up the geometry of the problem, we assume that the two chains are located in parallel planes. One chain is located in the  $y=0$  plane and follows the curve  $\{x, y, z\} = \{x, 0, z(x)\}$ . The second chain is located in the  $y=d$  plane and follows the curve  $\{x, y, z\} = \{x, d, -z(x)\}$ . The total electrostatic interaction energy of the two chains is given by

$$E_{\text{el}} = \frac{\xi^2}{l_B} \int_{-\infty}^{\infty} dx (1 + z_x^2)^{1/2} \times \int_{-\infty}^{\infty} dx' (1 + z_{x'}^2)^{1/2} \frac{e^{-\kappa r_{12}}}{r_{12}}, \quad (3)$$

where  $z_x \equiv dz/dx$  and

$$r_{12}^2 = [x - x']^2 + d^2 + [z(x) + z(x')]^2. \quad (4)$$

The bending energy of each chain is

$$E_{\text{bend}} = \frac{l_p}{2} \int_{-\infty}^{\infty} dx (1 + z_x^2)^{-5/2} z_{xx}^2. \quad (5)$$

The bending modulus of the chain is given by  $l_p k_B T$ , where  $l_p$  is the persistence length; correlations in the direction of the chain decay exponentially with a decay length  $l_p$ . The approximate persistence length of DNA is 500 Å in the double helix form.<sup>45</sup> Actin filaments are much more rigid and their persistence length is estimated to be between 2 and 18 μm. Generally speaking,  $l_p$  depends on the monomer–monomer interactions and these depend on the surrounding environment. Intrachain repulsions (e.g., Coulomb) can stiffen the chain and increase  $l_p$ ,<sup>37,42</sup> while attractions can “soften” it, reducing  $l_p$  and even leading to buckling instabilities.<sup>38–41</sup> In the following we will neglect variations in  $l_p$  and take it to be a fixed quantity.

## B. Interaction between two linkers

With the basic equations in hand, we are now equipped to examine how chain interactions lead to an effective interaction between two linkers. We start by considering two linkers connecting the two chains. In our model, the linkers are located at a distance  $l$  from each other and constrain each chain at two points so that  $z(\pm l/2) = 0$  [see Fig. 2(a)].

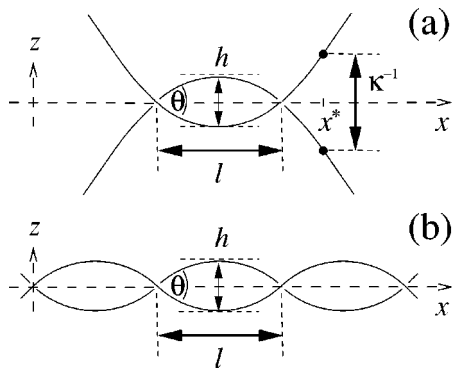


FIG. 2. (a) Typical conformation of two chains connected by two linkers at  $x = \pm l/2$ . The chains are curved between the linkers and straighten out as the distance between the chains increases beyond the electrostatic screening length. (b) Typical conformation of two chains connected by many linkers distributed at a fixed separation  $l$  from each other. In both cases, one chain is in the  $y=0$  plane while the other is in the  $y=d$  plane; the  $y$ -axis being perpendicular to the page.

While the two linkers constrain the position of each chain at two points, the interchain electrostatic repulsion exerts a torque on the free ends that bends the central section of the two chains [see Fig. 2(a)]. Far away from the linkers ( $|x| \gg l/2$ ) the two chains straighten out. A simple trial function that will capture these two features can be constructed by matching a parabolic profile for  $|x| \leq x^*$  with straight lines for  $|x| \geq x^*$ ,

$$z(x) = \begin{cases} \frac{h}{2}[1 - (2x/l)^2] & x \leq x^* \\ -\kappa^{-1}/2 - a(x - x^*) & x \geq x^* \end{cases}, \quad (6)$$

where  $x^*$  is chosen as the point where the vertical distance between the two chains exceeds  $\kappa^{-1}$ . Namely,  $z(x^*) = -\kappa^{-1}/2$  and consequently

$$x^* = \frac{l}{2} \sqrt{1 + 1/\kappa h}. \quad (7)$$

The slope  $a$  of the linear section is determined, by the continuity of the first derivative, to be

$$a = -\frac{2h}{l} \sqrt{1 + 1/\kappa h}. \quad (8)$$

The variational quantity  $h$  characterizes the geometry of the section between the two linkers, and is determined by minimizing the free energy  $f = E_{\text{bend}} + E_{\text{el}}$  from Eqs. (3) and (5).

The crosslink angle  $\theta$  can be determined from  $h$  through

$$\tan(\theta/2) = 2h/l, \quad (9)$$

whereas the apparent angle  $\theta^*$  is defined as the angle between the straight segments,

$$\tan(\theta^*/2) = a, \quad (10)$$

and can be different from the local angle  $\theta$ .

Typical interaction profiles are shown in Fig. 3, where the free energy  $f$  was minimized numerically with respect to  $h$ . The dependence of  $\theta$  on the interlinker distance is depicted as well. At large distances the two linkers are independent of each other—the chains are perpendicular in the

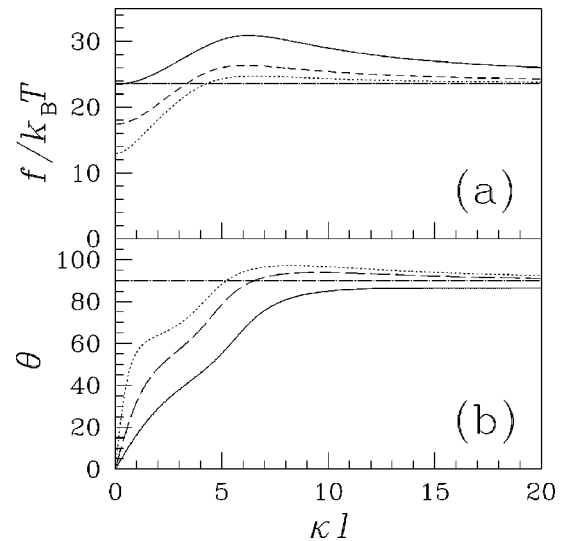


FIG. 3. Interaction free energy  $f$  (a) and crosslink angle  $\theta$  (b) as functions of the reduced distance  $\kappa l$  between the two linkers. The curves correspond to different values of the persistence length  $l_p = 10 \text{ \AA}$  (dots)  $l_p = 50 \text{ \AA}$  (dashed curve), and  $l_p = 200 \text{ \AA}$  (solid curve). The screening length is  $\kappa^{-1} = 10 \text{ \AA}$ , the effective Manning–Oosawa parameter  $\xi = 4$ , the interchain separation  $d = 25 \text{ \AA}$ , and the Bjerrum length  $l_B = 7 \text{ \AA}$ . The horizontal line in (a) marks the energy of two separate crosslinks  $f = 2\Gamma$ .

vicinity of the link ( $\theta \rightarrow \pi/2$ ) and the free energy is simply twice the energy of a single link ( $f \rightarrow 2\Gamma$ ). As the linkers move closer together the chains start to bend and the free energy increases. This bending energy is responsible for the repulsive barrier that can be observed in Fig. 3.

At large distances  $l \gg \kappa^{-1}$ , the electrostatic energy is dominated by the crosslink energies,

$$E_{\text{el}} \approx 2\Gamma / \sin \theta. \quad (11)$$

The bending energy can be approximated by taking a fixed radius of curvature between the two links,  $R = l \sin(\theta/2)/2$ . This yields

$$E_{\text{bend}} \approx 2 \frac{l_p}{l} \theta \sin(\theta/2). \quad (12)$$

Minimizing with respect to  $\theta$  at a fixed  $l$  yields the following implicit equation for  $\theta$ :

$$\sin(\theta/2) + \frac{\theta}{2} \cos(\theta/2) - \Gamma \frac{l \cos \theta}{l_p \sin^2 \theta} = 0. \quad (13)$$

Clearly, as  $\Gamma l/l_p$  increases  $\theta$  must reach  $\pi/2$ . Indeed, the results presented in Fig. 3 show that in the repulsive regime  $\theta \rightarrow \pi/2$ . The leading contribution to the free energy in this regime is therefore

$$f(l) \approx 2\Gamma + \alpha l_p/l, \quad (14)$$

where  $\alpha = \pi/\sqrt{2}$  is a numerical prefactor. The repulsive term increases with the persistence length, as can also be seen in the figure.

As the linkers move closer to each other the free energy increases until it reaches a maximum and then it decreases. The latter results from the partial overlap of the two chain junctions. In fact, at distances shorter than the screening length  $\kappa^{-1}$  the electrostatic energy should decrease from  $2\Gamma$

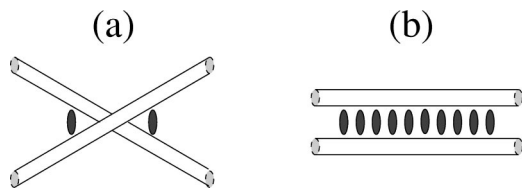


FIG. 4. Schematic view of a multiple-linker junction with two inter-chain linkers (a) and of two parallel sections with several linkers in between (b).

to  $\Gamma$  as the two crosslinks gradually merge. At these short distances  $2\Gamma$  overestimates the electrostatic contribution. The excess energy is due to the extra free ends of the two crosslinks. The interaction energy of these loose ends scales as  $\Gamma$  and decays as  $e^{-\kappa l}$  since the dimensions of the loop formed between the two linkers is of the order of  $l$ . The interaction free energy at short distances can be therefore approximated by

$$f(l) \approx \Gamma [2 - e^{-\kappa l}], \quad (15)$$

where we have neglected the bending energy term. This approximate expression interpolates between a single crosslink at short distances [ $f(l \rightarrow 0) \approx \Gamma$ ] and two crosslinks at large distances [ $f(l \rightarrow \infty) \approx 2\Gamma$ ].

### C. A chain of interacting linkers

The trial function used above for two linkers does not allow the free ends of the chains to exchange places. In other words, we neglect the possibility of the configuration sketched in Fig. 4(a). As a result, the two junctions remain distinct from each other even at very short distances and the chains must bend in the presence of the two linkers. As the number of linkers at a junction increases, we expect the preferred crossing angle at the junction to decrease, and to eventually approach zero.<sup>46</sup> In that limit, the junction becomes a straight section where the two chains are parallel and connected by many linkers [see Fig. 4(b)], and it can be viewed as a linear sequence of closely-spaced junctions. This is a many-linker effect. Instead of including many-linker interactions explicitly, we include them by extracting an effective pair interaction from a configuration that captures the essence of the many-linker effect. Specifically, we study an infinite crystal of linkers equally spaced at a distance  $l$  as shown in Fig. 2(b), and identify the resulting free energy per linker as the effective pair potential.

We choose a periodic trial function for the chain configurations of the form,

$$z(x) = \frac{h}{2} \cos(\pi x/l), \quad (16)$$

where  $h$  is a variational amplitude. The crosslink angle  $\theta$  is now given by  $\tan(\theta/2) = \pi h/2l$ . It should be emphasized that although the exact shape of the trial function affects the numerical values it should not have a qualitative effect on the results.

In Fig. 5 the free energy per linker is calculated by minimizing the sum of the electrostatic energy [Eq. (3)] and the bending energy [Eq. (5)] with respect to the displacement  $h$ . At large separations each crosslink is independent of its

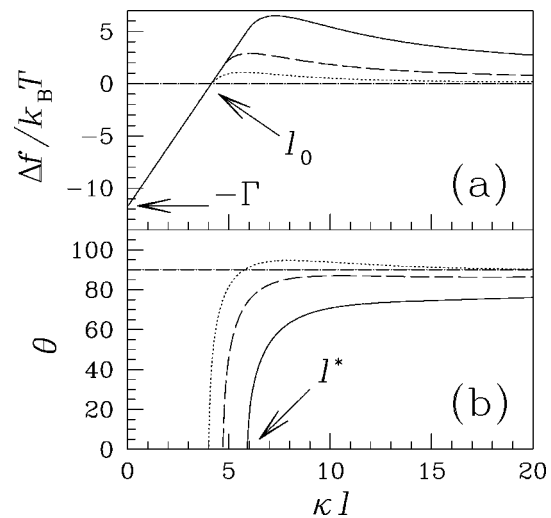


FIG. 5. Interaction free energies per crosslink  $\Delta f(l) = f(l) - \Gamma$  (a) and crossing angle  $\theta$  (b) as functions of the reduced distance  $\kappa l$  between the two linkers. Note that  $\Delta f$  changes sign for  $l = l_0$  and that  $\theta$  becomes nonzero at  $l = l^*$  (denoted by an arrow for the solid curve). The curves correspond to different values of the chain persistence length  $l_p = 10 \text{ \AA}$  (dots),  $l_p = 50 \text{ \AA}$  (dashed curve), and  $l_p = 200 \text{ \AA}$  (solid curve). The interchain separation is  $d = 25 \text{ \AA}$ , the effective Manning–Oosawa parameter  $\xi = 4$ , the screening length  $\kappa^{-1} = 10 \text{ \AA}$ , and the Bjerrum length  $l_B = 7 \text{ \AA}$ .

neighbors and contributes a term equal to  $\Gamma$ . It is therefore useful to subtract this constant from the interaction free energy and add it later to the chemical potential of the linkers. The resulting free energy  $\Delta f(l) = f(l) - \Gamma$  is plotted as a function of the reduced interlinker separation  $\kappa l$  in Fig. 5(a); the crosslink angle  $\theta(l)$  is plotted in Fig. 5(b).

At large separations the crosslink angle approaches  $90^\circ$  and the same approximation as before applies

$$f(l) \approx \Gamma + \alpha l_p/l \quad l \rightarrow \infty. \quad (17)$$

At short distances one crosslink is eliminated and the linkers gain energy by accumulating close to each other. In the limit  $l \rightarrow 0$  the energy gain is equal to  $-\Gamma$  per linker (indicated by an arrow on the figure). Furthermore, for relatively stiff chains, where  $l_p \gg \kappa^{-1}$  (as is the case in Fig. 5) the electrostatic interaction is not strong enough to bend the chains at short distances and the chains remain straight below a certain threshold distance  $l^*$ . Indeed, as demonstrated in Fig. 5(b), the crossing angle  $\theta$  vanishes for  $l \leq l^*$ . The crossover distance  $l^*$  can be estimated by considering small modulations in the  $z$  direction  $\Delta z = h \cos(\pi z/l)$  where  $h \ll d$ . The effect of these modulations is to locally increase the interchain distance, thus reducing the electrostatic energy,

$$\Delta E_{\text{el}}(l) \approx -\frac{2\xi^2 h^2 l}{d^2 l_B} K_1(\kappa d), \quad (18)$$

where  $K_1$  is the first order modified Bessel function. At the crossover the gain in the electrostatic energy exactly balances the bending energy,

$$\Delta E_{\text{bend}}(l) \approx \frac{\pi^4 h^2 l_p}{2l^3}. \quad (19)$$

Thus, the chains will bend as soon as  $\Delta E_{el} + \Delta E_{bend}$  becomes negative, which occurs for

$$l \geq l^* = \frac{\pi}{\sqrt{2}} \left( \frac{l_B l_p d^2}{\xi^2 K_1(\kappa d)} \right)^{1/4} \quad (20)$$

Using Eq. (20) for the data of Fig. 5 yields  $\kappa l^* \approx 3.1$  (for  $l_p = 10 \text{ \AA}$ ),  $\kappa l^* \approx 4.6$  (for  $l_p = 50 \text{ \AA}$ ), and  $\kappa l^* \approx 6.5$  (for  $l_p = 200 \text{ \AA}$ ). These estimates agree reasonably well with the results presented in the figure.

When the chains are straight, the interaction free energy per linker equals the length of the segment,  $l$ , times the electrostatic interaction energy (per unit length) of two infinite parallel cylinders,

$$f(l) \approx \frac{2\xi^2 K_0(\kappa d)}{l_B \kappa r_s K_1(\kappa r_s)} l \equiv \frac{\Gamma}{l_0} l \quad l \rightarrow 0. \quad (21)$$

where  $K_0$  is the zero order modified Bessel function. The linear dependence on  $l$  arises simply because the same electrostatic energy is divided between more linkers. Deviation from linear behavior enters as soon as  $l \approx l^*$  and the chains begin to deform. As the bending modulus increases (larger persistence length) it becomes more difficult to bend the chains and the linkers need to be further away from each other before the chains start to bend.

At  $l = l_0$  the interaction free energy equals its asymptotic value  $f(l_0) = f(l \rightarrow \infty) = \Gamma$ . In the limit  $d \gg \kappa^{-1} \gg r_s$ ,

$$l_0 \approx (2\pi d \kappa^{-1})^{1/2}. \quad (22)$$

For the parameters of Fig. 5 the above equation gives  $\kappa l_0 \approx 4$  in agreement with the results of the variational calculation.

As discussed in the next section, the attraction at short distances (in both regimes) can lead to accumulation of linkers between the two chains. The rate of this accumulation depends on the height of the repulsive barrier which is proportional to  $l_p/l^*$  and thus scales as  $l_p^{3/4}$ .

### III. THE ONE-DIMENSIONAL LINKER FLUID

#### A. Introduction

We proceed now to the full statistical mechanics of the many-linker system, including fluctuations in the interlinker separations. We use the interaction free energy calculated in the previous section as a contribution to the two body (effective) interaction energy between linkers. The full effective pair interaction contains three terms,

$$v(l_j) = \Delta f(l_j) + f_{loop}(l_j) + v_{direct}(l_j), \quad (23)$$

where  $l_j$  denotes the separation between linker  $j$  and linker  $j+1$ . Below, we discuss each of the terms in turn.

The first term in Eq. (23) is the indirect linker-linker interaction mediated by the two chains, calculated in the previous section. Note that we have subtracted the constant  $f(\infty) = \Gamma$  but will include it in the chemical potential. The interaction free energy  $\Delta f(l_j)$  was calculated in the preceding section for a perfectly periodic profile. Nevertheless, we use it here as an approximation for the nearest neighbor interaction in a disordered fluidlike structure. The error introduced by this approximation depends on the coupling be-

tween the chain section on one side of a linker and the chain section on the other side. At large linker separations  $l_j \gg \kappa^{-1}$  the crossing angle saturates to  $90^\circ$  and the two consecutive sections are decoupled from each other. In this regime, the interaction between linkers is indeed equal to the result calculated from the periodic case. At small linker separations, the approximation is again justified because the chains are straight (the crossing angle is  $0^\circ$ ). It is only for intermediate crossing angles that the decoupling assumption no longer holds. However, as shown in Fig. 5(b), the crossing angle crosses over from  $0^\circ$  to  $90^\circ$  over a very narrow range of inter-linker separations, so the intermediate regime is small.

The second term in Eq. (23) is the chain configurational entropy associated with the loop that is formed by the two chain sections connecting the two linkers. It gives rise to a logarithmic term of the form,<sup>30,47,48</sup>

$$f_{loop}(l_j) = c \ln[l/l_p], \quad (24)$$

where the exact value of  $c$  depends on the statistics of the chains. For ideal chains  $c = 3/2$ , while for a self-avoiding walk  $c = 7/4$ .<sup>47</sup> If excluded volume interactions between each loop and different parts of the chain are taken into account the coefficient becomes  $c \approx 2.1$ .<sup>48</sup> For semiflexible chains these values apply only at large separations  $l_j \gg l_p$ . When  $l_j$  is comparable to  $l_p$  the value of  $c$  is modified.<sup>31,33</sup> However, in this regime the contribution of the bending rigidity far exceeds the entropy of the loops. We can therefore neglect the deviations from the large distance behavior and assume that  $c = 3/2$  as long as  $l_j \geq l_p$  and that  $c = 0$  when  $l_j < l_p$ .

The loop entropy has important consequences in theoretical models of DNA denaturation.<sup>30,47,48</sup> It turns out that due to the long-ranged nature of the logarithm term, the coefficient can change the nature of the DNA melting transition from second order (when  $1 < c \leq 2$ ) to first order (when  $c > 2$ ). We expect excluded volume interactions to have a similar effect in our case as well. Namely, the rounded transition that is discussed below could turn into a first order phase transition if excluded volume interactions are fully accounted for.

The term  $v_{direct}(l_j)$  takes into account the bare linker-linker interactions. The main contributions to this term are the short range hard core interaction,

$$v_{HC}(l_j) = \begin{cases} \infty & l_j \leq b \\ 0 & l_j > b \end{cases} \quad (25)$$

and the screened Coulomb repulsion,

$$v_{zz}(l_j) = \frac{z^2 l_B}{l_j} e^{-\kappa l_j}. \quad (26)$$

The final approximation that we make is to treat the effective interaction, Eq. (23), at the nearest-neighbor level. Each of the three terms contains further neighbor contributions, but as we will argue below, these contributions will not change the qualitative phase behavior of the system.

In the first term, next-nearest-neighbor interactions do not exist when the crossing angle is  $0^\circ$  (short separations) or  $90^\circ$  (large separations). As explained above, neighboring sections separated by a junction are decoupled in these two limits. In the intermediate regime, there are further neighbor interactions, but because they are at intermediate separations, they are not long-ranged and therefore do not affect phase behavior. We note in passing that although the first term contains a  $1/l$  repulsive tail, it cannot lead to crystallization for a similar reason: when  $l$  is large and the linkers are far apart, the crossing angle is  $90^\circ$  and the interactions do not extend beyond the nearest neighbor. Thus, the first term cannot stabilize the one-dimensional crystal of linkers against fluctuations.<sup>49</sup>

In the second term, next-nearest-neighbor interactions can arise when loops interact with each other because of excluded volume interactions between chains. To our knowledge, this effect has not been taken into account even within sophisticated treatments of the DNA denaturation problem,<sup>48</sup> and we do not attempt to include it here.

Finally, the third term includes direct interactions such as the Coulomb interaction. We take the Coulomb interaction into account only at the nearest-neighbor level. We note that the presence of the two oppositely charged chains provides a neutralizing background to the charged linkers, so the system is a one-component plasma in one dimension interacting via three-dimensional screened Coulomb interactions. Because the interactions are screened, they cannot stabilize the one-dimensional crystal against fluctuations. Thus, higher-neighbor interactions cannot change the phase behavior of the system and can therefore be neglected.

## B. Statistical mechanics of a one-dimensional linker fluid

We proceed now to extract the thermodynamic properties of a linker fluid from the effective interlinker interaction  $v(l_j)$ . The number of linkers is  $N$  and they are restricted to a section of length  $L$  between the two chains. The natural microscopic degrees of freedom are the linker positions  $\{x_j\}$ , where  $0 < x_1 < x_2 < \dots < x_N < L$ .

If only nearest neighbor interactions are considered, it is convenient to express the partition function of the system in terms of the interlinker distances  $l_j = x_{j+1} - x_j$ . Two virtual particles can be added at  $x_0$  and  $x_{N+1}$  that do not interact with the linkers so that  $v(l_0) = v(l_N) \equiv 0$ . In the canonical ensemble where  $N$  and  $L$  are fixed, the set of variables  $\{l_j\}$  satisfies the constraint  $l_0 + l_1 + l_2 + \dots + l_N = L$ . The integrals over the  $l_j$ 's can be decoupled from each other in the Gibbs ensemble where the one-dimensional pressure  $P$  is the natural variable instead of  $L$ .<sup>49</sup> The pressure is equivalent to a Lagrange multiplier ensuring that the volume (length) constraint is satisfied only *on the average* and the size of the system is equal to  $L$  in the thermodynamic limit  $N, L \rightarrow \infty$ . In this limit, the choice of the ensemble for the calculation is a matter of convenience as each of the thermodynamic potentials can be transformed to any of the other potentials by means of a Legendre transform.

In the Gibbs ensemble the partition function is

$$Z_N = \int_0^\infty \frac{dl_0}{\lambda_T} \dots \int_0^\infty \frac{dl_N}{\lambda_T} \exp\left(-\sum_{j=0}^N v(l_j) - P \sum_{j=0}^N l_j\right) \\ = Z_0^2 Z_1^{N-1}, \quad (27)$$

$$Z_0 = \int_0^\infty \frac{dl_0}{\lambda_T} \exp(-Pl_0) = \frac{1}{\lambda_T P}, \quad (28)$$

$$Z_1 = \int_0^\infty \frac{dl}{\lambda_T} \exp(-v(l) - Pl), \quad (29)$$

where  $\lambda_T$  is a microscopic length scale and originates from tracing over the kinetic degrees of freedom. An extra factor of  $\lambda_T$  is included in order to keep  $Z_N$  dimensionless.

The Gibbs potential is now given by

$$G(N, P, T) = -\ln Z_N = -(N-1) \ln Z_1 - 2 \ln Z_0, \quad (30)$$

and size of the system is

$$L(N, P, T) = -\frac{1}{Z_N} \frac{\partial Z_N}{\partial P} = \frac{\partial G}{\partial P}. \quad (31)$$

The one-dimensional pressure  $P$  has dimensions of force. It can be interpreted as the thermal average of the force acting on each linker from both sides. If the system were to be confined to a long narrow tube of length  $L$ ,  $P$  would also be the force acting on the two caps at the far ends of the tube.

Additional thermodynamic information can be extracted from the partition function and the Gibbs potential. For example, the chemical potential of the linkers can be calculated as

$$\mu = \frac{G}{N} = -\left(1 - \frac{1}{N}\right) \ln Z_1 - \frac{2}{N} \ln Z_0 \xrightarrow{N \rightarrow \infty} -\ln Z_1, \quad (32)$$

and the average interlinker distance is given by

$$\bar{l} \equiv \langle l \rangle = \frac{1}{Z_1} \int_0^\infty \frac{dl}{\lambda_T} l \exp(-v(l) - Pl) \quad (33)$$

from which the linker density  $\rho = 1/\bar{l}$  can be easily extracted. Another important parameter is the mean-square fluctuation in the interlinker distance,

$$\Delta l^2 = \langle l^2 \rangle - \bar{l}^2 \\ = \frac{1}{Z_1} \int_0^\infty \frac{dl}{\lambda_T} l^2 \exp(-v(l) - Pl) - \bar{l}^2. \quad (34)$$

In the thermodynamic limit  $N \rightarrow \infty$ , the compressibility is directly related to  $\Delta l^2$  via

$$\kappa_T = -\frac{1}{L} \frac{\partial L}{\partial P} = \frac{\Delta l^2}{\bar{l}}. \quad (35)$$

Finally, one can also calculate the probability density  $p(l)$  of two linkers being at a distance  $l$ ,

$$p(l) = \frac{1}{Z_1} \frac{1}{\lambda_T} e^{-v(l) - Pl}. \quad (36)$$

In principle, Eq. (31) can be inverted to give the pressure  $P$  as function of the chain length  $L$ . Due to extensivity in the thermodynamic limit,  $P$  can only be a function of the linker

density  $\rho = N/L$ . Via Legendre transformation it is then possible to return to the canonical ensemble and calculate the free energy of the system for a fixed number of particles and a fixed chain length,

$$F(N, L, T) = G - PL, \quad (37)$$

$$f(\rho, T) \equiv \frac{F}{L} = \rho\mu - P.$$

This ensemble reflects the situation encountered in experiments that are performed at high enough chain concentrations so that all condensing agents are in the close vicinity of the chains. The number of linkers is basically determined by the ratio between the number of condensing agents and the number of chains in solution.

Similarly, one can also calculate the grand canonical potential for a fixed chemical potential and fixed chain length,

$$\Omega(\mu, L, T) = F - \mu N = -PL, \quad (38)$$

$$\omega(\mu, T) \equiv \frac{\Omega}{L} = -P.$$

This ensemble corresponds to experiments performed at low chain concentrations where the number of condensing agents in the surrounding solution is not affected by the presence of the chains. The linkers can then be considered to be in equilibrium with a reservoir of fixed concentration.

Finally, we recall that in our definition of the interaction potential  $v(l)$  we have omitted two terms that should be recovered in the chemical potential. The total chemical potential should therefore read

$$\mu_{\text{tot}} = \mu - 2\varepsilon_0 + \Gamma, \quad (39)$$

where  $2\varepsilon_0$  is the linker adsorption energy between the two chains and  $\Gamma$  is the electrostatic energy associated with a new crosslink. If the linkers are in contact with a reservoir (bulk) of linkers at a fixed concentration  $c_l$  the total chemical potential must equal that of the bulk,

$$\mu_{\text{tot}} = \mu_b \equiv \ln c_l \lambda_T^3, \quad (40)$$

where  $\lambda_T$  is the thermal wave length of the linkers in solution. The grand canonical potential  $\omega(\mu)$  is unaffected by our definition of the chemical potential, while the total canonical free energy becomes

$$f_{\text{tot}}(\rho) = f(\rho) + (\Gamma - 2\varepsilon_0)\rho. \quad (41)$$

An exact estimate of  $\varepsilon_0$  has to take into account the structure of the counterion layer between the two chains and, in particular, the competitive adsorption of monovalent and multivalent counterions.<sup>44,50</sup> A rough estimate based on the interaction of polyvalent counterions with an isolated charged rod in a salt-free solution gives  $\varepsilon_0 \approx 2z\xi$ . In order to limit the number of assumptions made, we will present our results in terms of  $\mu$  and  $f$  instead of  $\mu_{\text{tot}}$  and  $f_{\text{tot}}$ .

### C. Numerical results

The interaction potentials obtained using the variational method (see Fig. 5) can be used as a starting point for calculating the thermodynamic properties of the linker fluid. A

typical example is presented in Fig. 6, where we have used the same values for the physical quantities as in Fig. 5 (long dashed curve) and in addition we have chosen  $b = 1 \text{ \AA}$  and  $\lambda_T = 1 \text{ \AA}$ . The different sets of curves correspond to different linker valencies. The solid curves correspond to neutral linkers with only hard core interactions ( $z = 0$ ), while the short (long) dashed curves correspond to counterion valency  $z = 2$  ( $z = 3$ ).

In Fig. 6(a), the free energy density  $f(\rho)$  is plotted as a function of the linker density. The linker density  $\rho$  is a natural variable when the number of linkers is fixed. Physically, such a situation occurs at high chain densities when there are not enough condensing agents in the solution. As long as the free energy can be lowered by forming additional links, any condensing agents that are present in the solution will form interchain links. This process will stop as soon as the minimum in the free energy is reached. As demonstrated in Fig. 6(a), the position of this minimum depends on the nature of the interlinker interactions. Neutral linkers saturate at the close packing density  $\rho = 1/b$  while charged linkers saturate at much lower densities.

Note that the free energy is concave with no singularity, i.e., the model system does not undergo a first order phase transition. The absence of such a transition is a consequence of the fact that only nearest-neighbor interactions are taken into account. Yet, even though the system does not undergo a true phase transition in the thermodynamic sense, the crossover can be quite sharp. In Fig. 6(b) the linker density  $\rho$  is plotted as a function of the chemical potential  $\mu$ . When  $z = 0$ , a sharp jump in the density occurs close to the point where  $\mu \approx -\Gamma$ , where  $\Gamma \approx 11.8$  for the parameters of Fig. 6. Below this point the linkers are dispersed far from each other and the chains form large loops in between. Above this point the linkers are much closer to each other and the chains are almost parallel to each other, resembling a railway track. This sharp jump appears as an almost linear section in the free energy [Fig. 6(a)] in the range  $0 \leq \rho \leq 0.2$ .

The increase in the density is accompanied by large fluctuations in the interlinker separation  $\Delta l$  as depicted in Fig. 6(c). These large fluctuations are due to the coexistence of small and large interlinker separations at the crossover, similar to those present in the vicinity of a first order transition. Note that we have neglected excluded volume interactions between different parts of the chain that contribute to a long-range interaction between different parts of the chain. It has been shown recently<sup>48</sup> in the context of DNA denaturation that this effect leads to a first order transition.

In Fig. 6(d) the grand canonical potential  $\omega(\mu)$  is plotted as a function of the chemical potential. The choice of this ensemble is appropriate at low chain concentrations and when the number of linkers in the solution is large enough for it to be considered a reservoir of linkers with fixed chemical potential. As the system enters the high density regime the grand canonical potential decreases and as a result pairs of chains become more favorable with respect to unpaired chains. The correspondence between the ‘‘railway track’’ phase and chain pairing is important since the formation of chain pairs marks the onset of bundling.

If the linkers are charged, the strong interlinker Coulomb

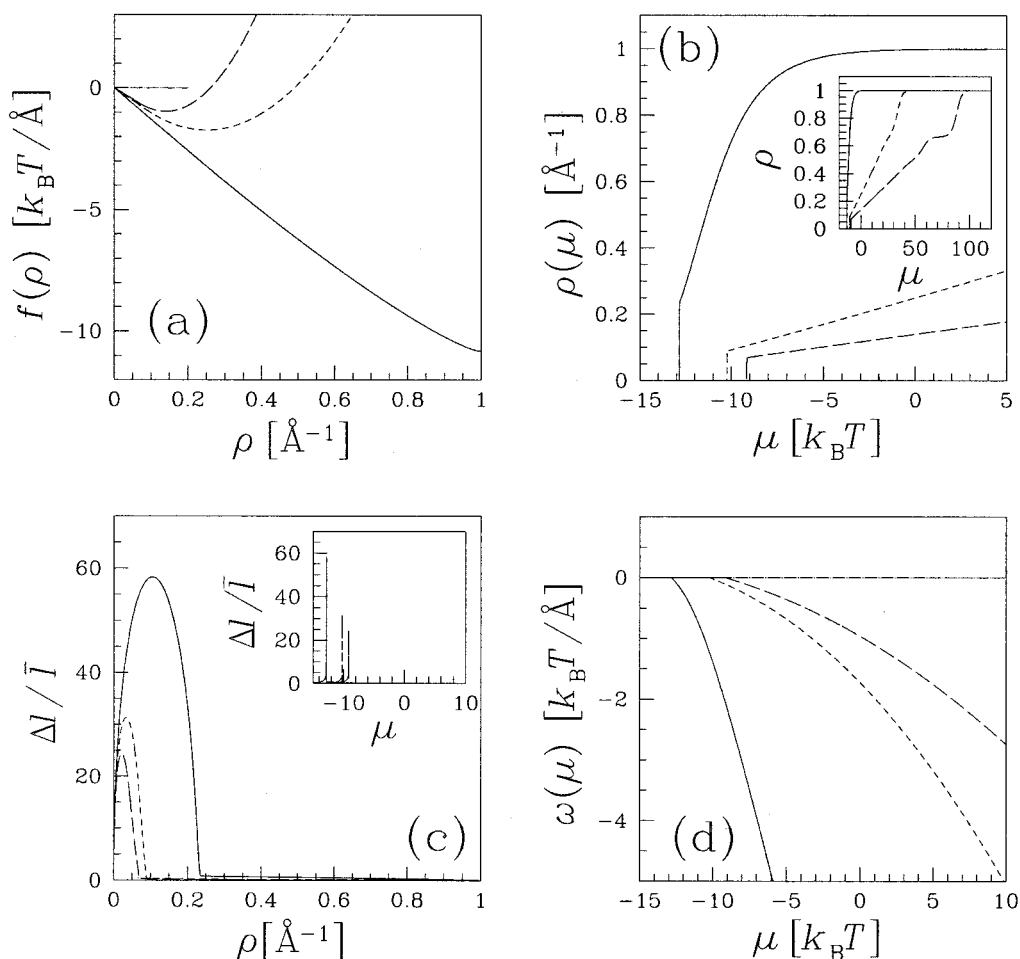


FIG. 6. Thermodynamic potentials calculated numerically: (a) free energy density  $f(\rho)$  as a function of the linker density  $\rho$ ; (b) linker density  $\rho$  as a function of the chemical potential  $\mu$ ; (c) the fluctuations in the interlinker separation  $\Delta/\bar{l}$  as a function of  $\rho$  and  $\mu$  (inset); (d) grand canonical potential density  $\omega(\mu)$  as a function of the chemical potential  $\mu$ . The different curves correspond to different values of the linker valency:  $z=0$  (uncharged linkers, solid curve),  $z=2$  (short dashes), and  $z=3$  (long dashes). The values of the physical quantities used in the calculation are  $d=25 \text{ \AA}$ ,  $\xi=4$ ,  $\kappa^{-1}=10 \text{ \AA}$ ,  $l_B=7 \text{ \AA}$ ,  $l_p=50 \text{ \AA}$ ,  $b=1 \text{ \AA}$ , and  $\lambda_T=1 \text{ \AA}$ .

repulsion shifts the crossover point to higher chemical potentials and it becomes more difficult to push the linkers into the dense phase. As can be seen in Fig. 6(b) the increase in the linker density is much more moderate and consists of two additional jumps at high values of  $\mu$ . Note, however, that the initial crossover point is only slightly affected by the Coulomb repulsions and that the dominant changes happen above this point. Following the first jump, the density increases more or less linearly with the chemical potential. The average slope in this regime is approximately  $1/2z^2 l_B$  as predicted by simple analytical approximations presented in the Appendix. In two regions,  $0.5 \text{ \AA}^{-1} \leq \rho \leq 0.65 \text{ \AA}^{-1}$ , and  $0.65 \text{ \AA}^{-1} \leq \rho \leq 1 \text{ \AA}^{-1}$ , the slope becomes steeper and a relative increase in the fluctuations [Fig. 6(c)] can be also observed. These are typical signatures of a structural change which might be related to the hard-core interlinker repulsion since it is almost independent of the linker valency.

In the canonical ensemble the minimum of the free energy is no longer at close packing but at a much lower linker density [Fig. 6(a)]. The optimal density decreases with increased linker charge due to the enhancement of the direct linker-linker Coulomb repulsion. Similarly, the grand ca-

nonical potential is much less negative when compared to neutral linkers [Fig. 6(d)].

As we have seen previously, simple expressions can be derived that characterize the interlinker interaction in several limiting cases. We use these approximations, described in detail in the Appendix, to calculate the free energy of the system in the different regimes, and compare these results there to the numerical results reported above.

#### D. Chain pairing

Until now we have studied the distribution of linkers between the two chains assuming that *the two chains are paired, i.e., held together*. In fact, the chains will only stay close to each other if the free energy of the two-chain complex is lower than that of two isolated chains. We now compare the two possibilities—isolated chains versus chain complexation—and seek the point where pairing occurs.

The free energy of the two chain complex was presented previously while the free energy of the single chains can be estimated as follows: the chains adsorb multivalent counterions and the interaction between these adsorbed counterions

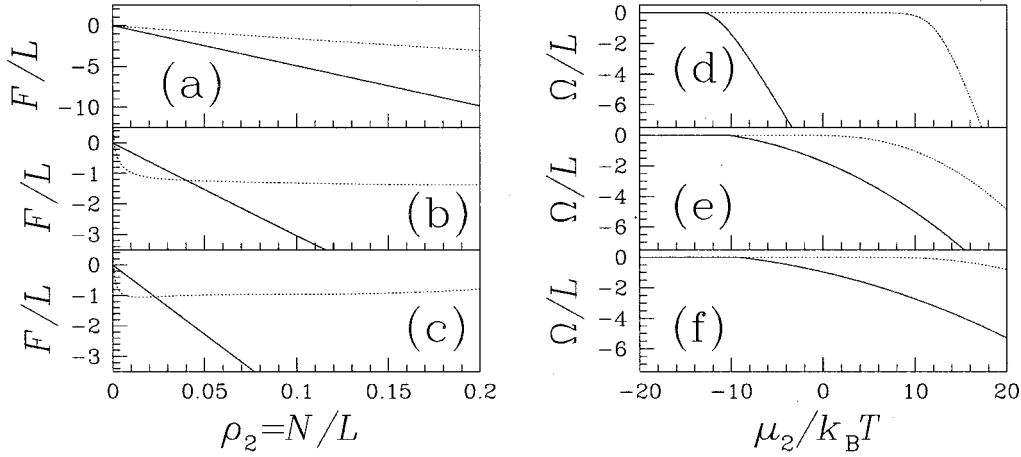


FIG. 7. Comparison of the free energy and grand canonical potential of a linkers fluid between paired chains (solid curves) and multivalent counterions adsorbing to isolated chains (dotted curves). The free energy per unit length  $F/L$  is plotted as a function of the density in the paired state  $\rho_2 = N/L$  in (a), (b), and (c). In (d), (e), and (f) the grand canonical potential per unit length  $\Omega/L$  is plotted on a logarithmic scale as a function of the chemical potential of the free linkers. The same values of the physical quantities as in Fig. 6 are used here. The hard core diameter and multivalent counterion valencies are  $b = 1 \text{ \AA}$ ,  $z=0$  in (a) and (d);  $b=0$ ,  $z=2$  in (b) and (c);  $b=0$ ,  $z=3$  in (e) and (f). The value  $z=3$  was used for calculating  $\epsilon_0$  in (a) and (d).

consists only of the direct part  $v_{\text{linker}}(l)$  of the interlinker potential [Eq. (23)]. The total length of the system is now  $2L$  and if the number of linkers is fixed the density of adsorbed counterions will be half the linker density in the paired state  $\rho_1 = \rho_2/2$ . Note that in the paired state, we have neglected the contribution of adsorbed counterions that do not form links between the two chains.

The same analytic approximations as discussed in the Appendix in detail can be applied here and yield the following thermodynamic properties. In the presence of hard-core interactions,

$$\mu = \ln\left(\frac{\lambda_T \rho_1}{1 - \rho_1 b}\right) + \frac{\rho_1 b}{1 - \rho_1 b} - \epsilon_0, \quad (42)$$

$$\frac{F}{2L} = \rho_1 \left[ \ln\left(\frac{\lambda_T \rho_1}{1 - \rho_1 b}\right) - 1 \right], \quad (43)$$

$$\frac{\Omega}{2L} = -\frac{\rho_1}{1 - \rho_1 b} - \rho \epsilon_0. \quad (44)$$

Similarly, Eqs. (A21), (A22) can be generalized in a straightforward way.

In Fig. 7 the free energy and grand canonical potential in the paired state are compared with the reference state of isolated chains. For comparison, the thermodynamic potentials and the number of particles are divided by the same length scale  $L$ . The chemical potentials are calculated using a crude approximate adsorption energy  $\epsilon_0 \approx 2z\xi$ . The data from Fig. 6 were used for the paired system.

As can be seen in the figure, the point where the paired state becomes favorable to the unpaired state almost coincides with the crossover from the dilute linker fluid to the dense fluid. We conclude that pairing occurs when  $\ln c_l \lambda_T^3 \approx -2\epsilon_0$ .

## IV. MOLECULAR DYNAMICS SIMULATIONS

### A. Introduction

In order to explore further our numerical model, we have performed molecular dynamics simulations of an overall neutral system consisting of two charged semiflexible chains and a mixture of monovalent ( $z=1$ ) and trivalent ( $z=3$ ) counterions with no co-ions (see Fig. 8).

Each chain consists of 64 charged monomers carrying one unit charge per monomer. All particles in the system (monomers and free ions as well) repel each other through a repulsive Lennard-Jones (LJ) potential,

$$U_{\text{LJ}}(r) = \begin{cases} 4\epsilon_{\text{LJ}} \left[ \left(\frac{\sigma}{r}\right)^{12} - \left(\frac{\sigma}{r}\right)^6 + \frac{1}{4} \right] & r \leq r_c = 2^{1/6}\sigma \\ 0 & r > r_c \end{cases}, \quad (45)$$

where  $\epsilon_{\text{LJ}}$  and  $\sigma$  are the LJ energy and length scales, respectively. The chain bond potential is the standard finite extensible nonlinear elastic (FENE) potential,

$$U_{\text{FENE}}(r) = -\frac{1}{2}k_0 r_0^2 \ln[1 - r^2/r_0^2] \quad (46)$$

with a spring constant  $k_0 = 7\epsilon_{\text{LJ}}/\sigma^2$  and maximal extension  $r_0 = 2\sigma$ . The simulations are performed at a fixed temperature  $k_B T = 1.2\epsilon_{\text{LJ}}$ , where the average bond size is  $\langle r \rangle = 1.1\sigma$ . Chain rigidity is introduced by the sum of angle dependent harmonic potentials,

$$U_{\text{bend}}(\theta) = k_1(\theta - \pi)^2. \quad (47)$$

Here  $\theta$  is the angle between neighboring bonds and  $k_1 = 20\epsilon_{\text{LJ}}/\text{rad}^2$ , which corresponds in our simulations to an intrinsic persistence length  $l_p \approx 18\sigma$ . Finally, the Coulomb interaction between pairs of charged particles of valency  $z_i$ ,  $z_j$  is given by

$$U_{\text{Coulomb}}(r)/k_B T = z_i z_j l_B / r, \quad (48)$$

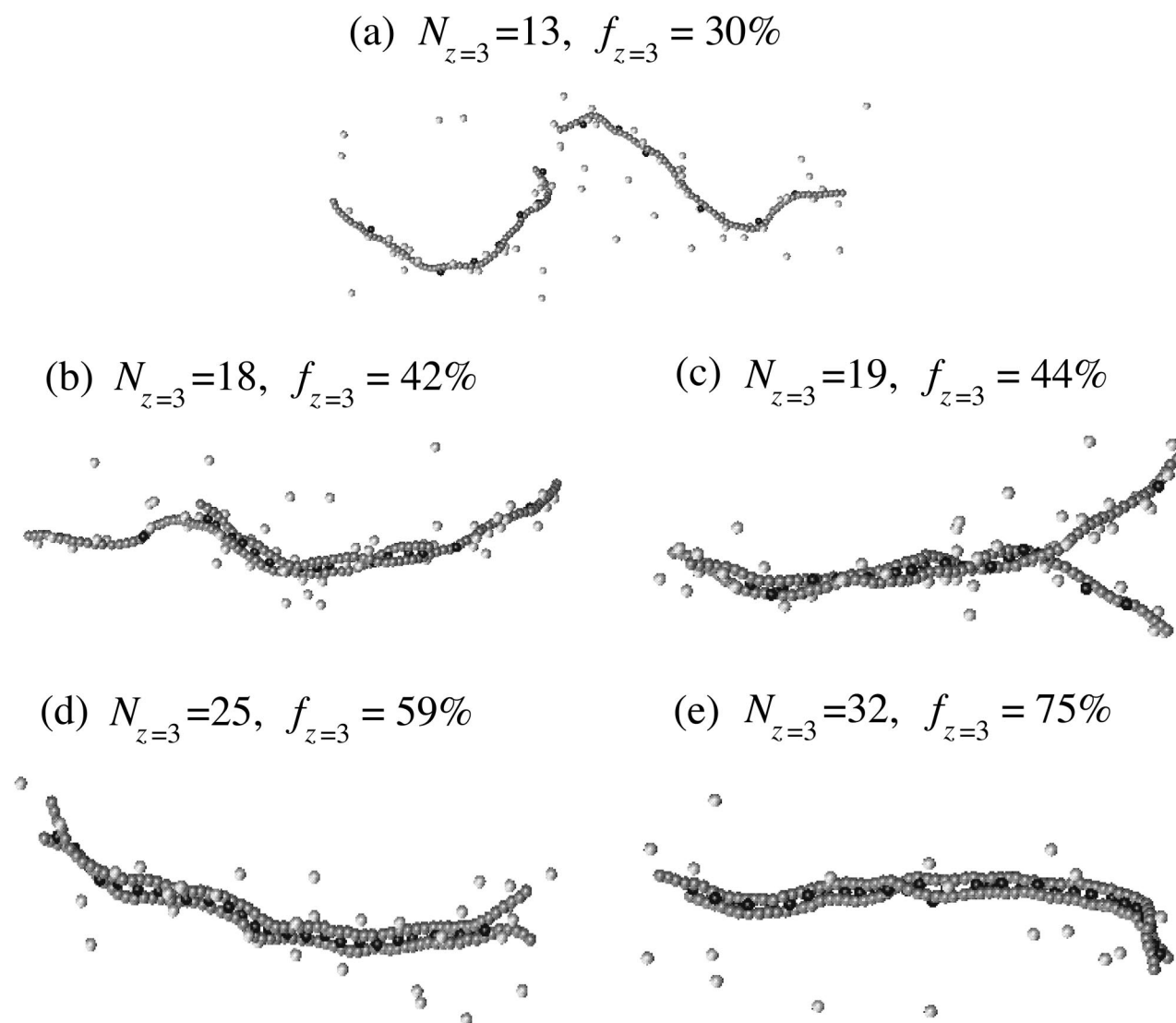


FIG. 8. Typical snapshots of the molecular dynamics simulations at different compositions: (a) isolated chains at  $N_{z=3} = 13$ ; (b) partial chain overlap at  $N_{z=3} = 18$ ; (c) metastable “fork” structure at  $N_{z=3} = 19$ ; (d) fully zippered structure at  $N_{z=3} = 25$ ; and (e) saturated structure at  $N_{z=3} = 32$ . The black spheres are trivalent counterions, the white spheres are monovalent ones, and the gray spheres are the monomers. The figure was prepared using VMD.<sup>52</sup>

and is calculated with periodic boundary conditions using the particle–particle particle–mesh (PPPM) algorithm<sup>51</sup> with a mesh consisting of  $16^3$  points. The Bjerrum length is  $l_B = 3.2\sigma$  and the Manning–Oosawa parameter characterizing the linear charge density along the chains is  $\xi = l_B / \langle r \rangle \approx 2.9$ . The simulations were performed in a cubic cell of dimensions  $(109\sigma)^3$ .

The dynamics of the system are performed with a Langevin thermostat.<sup>53</sup> Namely,  $m\dot{\mathbf{v}} = -m\gamma\mathbf{v} + \mathbf{f}^{(U)} + \mathbf{f}^{(T)}$ , where  $\mathbf{v}$  is the velocity of a particle (chain monomers as well as monovalent and trivalent ions),  $m$  its mass (identical for all particles), and  $\mathbf{f}^{(U)}$  the total force acting on it as a result of the potentials described above. The random (thermal) force  $\mathbf{f}^{(T)}$  satisfies  $\langle \mathbf{f}_i^{(T)} \rangle = 0$  and  $\langle \mathbf{f}_i^{(T)} \mathbf{f}_j^{(T)} \rangle = 6m\gamma k_B T \delta_{ij} / \Delta t$  at discrete time steps  $t_n = n\Delta t$ ;  $\gamma$  is the friction coefficient of the particles in the solution. The system is advanced in time steps  $\Delta t = 0.015\tau_{LJ}$  with  $\tau_{LJ} = \sigma\sqrt{m/\epsilon_{LJ}}$  being the basic Lennard-Jones time unit, while the damping constant is taken as  $\gamma = 1/\tau_{LJ}$ .

## B. Results

The main aim of the simulations was to probe the stability of two-chain complexes at different counterion mixtures. The initial configurations consisted of two chains next to each other and the counterions (monovalent and trivalent) closely near by. Since the total number of charged monomers is 128 the number of trivalent counterions can vary between 0 and 42. When the two chains are initially separated from each other they do not form a two-chain complex even at counterion mixtures where the complex appears to be stable. This can be attributed to a high kinetic barrier for aggregation similar to the one suggested for the bundling of rigid rods.<sup>54</sup> Due to this limitation we can only interpret our results in terms of the stability of the two-chain complex and we can not determine whether the complex is indeed the global minimum of the system or just a local one.

Another limitation of the simulation resides in the choice of the simulation box size, which corresponds to the concen-

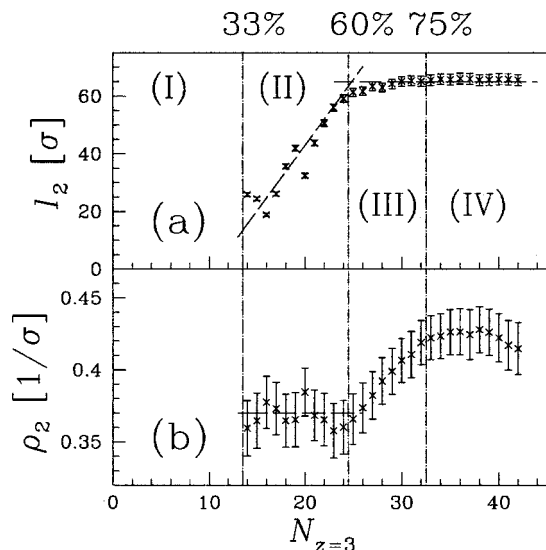


FIG. 9. The length of the segment shared by the two chains  $l_2$  (a) and the density of trivalent counterions  $\rho_2$  in this segment (b) as functions of the total number of trivalent counterions in the system  $N_{z=3}$ . See text for discussion of the four different regimes.

tration of chains in solution. The results of the simulation do depend on the box size since translational entropy of the chains depends logarithmically on the box size. In fact, at very low concentrations (large box size) the low osmotic pressure of the chains will pull them apart. On the other hand at large concentrations many chain effects become important. We have chosen an intermediate box size for which both these effects are minimal. Our choice is somewhat arbitrary and affects the results presented here quantitatively but not qualitatively.

Typical snapshots from the simulations are shown in Fig. 8, while a quantitative analysis is presented in Fig. 9. The fraction of chain charge (128) neutralized by trivalent counterions is given in each case by

$$f_{z=3} = \frac{3N_{z=3}}{3N_{z=3} + N_{z=1}} = \frac{3N_{z=3}}{128}. \quad (49)$$

Four different regimes can be distinguished depending on the number of trivalent counterions in the system. At low trivalent counterion numbers,  $N_{z=3} < N^* = 14$ , the chains do not remain together, and are basically isolated [see Fig. 8(a)]. In this first regime (I) less than one third of the monomer charges are balanced by the trivalent counterions ( $f_{z=3} \lesssim f^* = 33\%$ ).

At intermediate trivalent counterion numbers  $N^* \lesssim N_{z=3} \lesssim N^{**} \approx 24$  ( $f^* \lesssim f_{z=3} \lesssim f^{**} = 60\%$ ) the chains start to form a paired complex [see Fig. 8(b)]. Pairing is partial with the two chains being shifted with respect to each other (regime II). We note that some meta-stable structures such as the “fork” shown in Fig. 8(b) appear occasionally during the simulation. Such a structure is less favorable energetically as compared to the “shifted” structure [see, e.g., Fig. 8(b)], due to the electrostatic energy associated with the branching point.

In Fig. 9 the length of the shared segment  $l_2$  and the density  $\rho_2$  of trivalent counterions in this segment are plotted

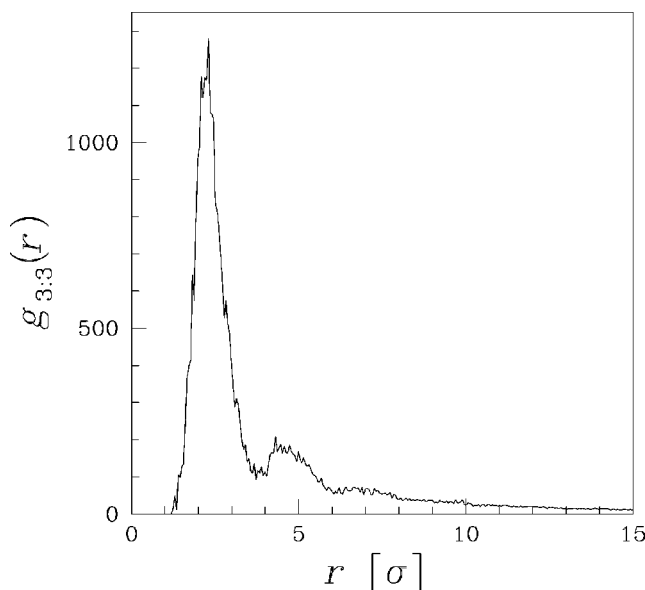


FIG. 10. Trivalent ion correlation function  $g_{3:3}(r)$  for  $N_{z=3} = 25$ .

as functions of the total number of trivalent counterions in the system. The length of the shared section  $l_2$  is calculated by first identifying the left and right neighbors of each shared multivalent counterion, and then summing up the interlinker separations. The density is simply the inverse of the average interlinker separation. First, note that the structure of the shared segment confirms that the trivalent counterions can be viewed as interchain linkers connecting the two chains. In the shared segment the two chains are as close to each other as they can be while accommodating trivalent counterions (“linkers”) in between. Although some monovalent counterions are in close proximity to the two chains they only rarely squeeze in between the two chains.

Second, it is clear from Fig. 9 that in this regime the density of interchain linkers remains more or less constant even as the total number of multivalent counterions is increased. Furthermore, the trivalent–trivalent correlation function  $g_{3:3}(r)$  defined as

$$g_{3:3}(r) = \frac{V}{4\pi r^2 N_{z=3}^2} \sum_{i \neq j} \langle \delta[r - |\mathbf{r}_i - \mathbf{r}_j|] \rangle \quad (50)$$

does not change drastically as the total number of trivalent counterions varies. A typical correlation function (corresponding to  $N_{z=3} = 25$ ) is plotted in Fig. 10. The principal features are the main peak around  $r \approx 2.5\sigma$  and the secondary peak around  $r \approx 4.5\sigma$ . The presence of these two peaks is a signature of short range liquidlike ordering of the trivalent counterions in between the two chains.

Constant linker density with increasing number of linkers in the system is a typical signature of phase coexistence. In our case the two phases are (i) trivalent counterions adsorbing at density  $\rho_1$  onto unpaired chain sections of total length  $2l_1$  and (ii) trivalent counterions serving as linkers at density  $\rho_2$  in the shared chain section of length  $l_2$ . At coexistence, both phases must share the same chemical potential and osmotic pressure,

$$\mu_1(\rho_1) = \mu_2(\rho_2), \quad (51)$$

$$2P_1(\rho_1) = P_2(\rho_2). \quad (52)$$

The solution of these two equations gives the optimal densities  $\rho_1^*$ ,  $\rho_2^*$  which must remain constant in the coexistence regime. The number of trivalent counterion in each of the phases  $N_1$ ,  $N_2$  as well as the lengths the unpaired sections ( $l_1$ ) and the shared section ( $l_2$ ) can be extracted from the following set of equations:

$$\rho_1^* = N_1 / l_1, \quad (53)$$

$$\rho_2^* = N_2 / l_2, \quad (54)$$

$$N_{z=3} = 2N_1 + N_2, \quad (55)$$

$$l_{\text{tot}} = l_1 + l_2. \quad (56)$$

The solution yields a linear dependence of the shared length on the number of polyvalent counterions (the ‘‘lever rule’’),

$$l_2 = \frac{N_{z=3} - 2l_{\text{tot}}\rho_1^*}{\rho_2^* - 2\rho_1^*}. \quad (57)$$

As can be seen in Fig. 9(a),  $l_2$  is indeed a linear function of  $N_{z=3}$  in regime II. The dashed line is drawn using the above equation with the following estimates:  $\rho_1^* \approx 0.075\sigma^{-1}$ ,  $\rho_2^* \approx 0.37\sigma^{-1}$ , and  $l_{\text{tot}} = 70.4\sigma$ .

It is interesting to compare this regime with the results of the theoretical model where we had two different transitions: (i) the crossover of the one-dimensional linker fluid from a dilute to a dense phase, and (ii) the chain pairing transition. Due to computational constraints we are limited in the simulations to relatively short chains. As a result, we cannot observe the large loops that should accompany the transition from the dilute linker fluid to the dense phase since the loops are expected to be longer than the chains themselves. The unpaired sections observed in the simulation are therefore reminiscent of two different features of the theoretical model: (i) the large loops characteristic of the intermediate linker phase; and (ii) unpaired chains coexisting with paired chains at the pairing point.

The coexistence regime ends around  $N_{z=3} \approx N^{**}$  when about 60% of the monomer charges are balanced by trivalent counterions. At this point the two chains are almost fully paired and the unpaired sections disappear [Fig. 8(c) and regime III in Fig. 9]; any addition of trivalent counterion is accompanied by an increase in the linker density. Finally, when  $N_{z=3} \geq N^{***} \approx 32$  (75% charge neutralization) the interlinker Coulomb repulsion makes it unfavorable to further squeeze trivalent counterions between the two chains and the extra counterions are excluded from the region between the two chains. In this regime the linker density saturates to its maximal value and does not increase further. The extra counterions do not diffuse far away from the chains but remain in the close vicinity of the two chain complex.

## V. DISCUSSION AND CONCLUSIONS

### A. Summary of pairing phenomena

In this paper we have studied the association of two charged semiflexible chains due to the presence of multivalent counterions or proteins serving as interchain linkers. Our main results can be summarized as follows.

First, we have studied the effective interlinker interaction due to the presence of the chains. We find that the combination of chain rigidity and interchain electrostatic repulsion leads to an effective potential that is repulsive at large interlinker separations and attractive at short separations.

We then used this potential together with the direct interlinker interaction (namely, the short-range hard-core repulsion and/or the screened Coulomb interaction) to study the behavior of a (quasi) one-dimensional linker fluid located in between the two chains. We find three different regimes depending on the density of linkers between the two chains; at low densities the linkers are in a dilute phase where isolated linkers are connected by large loops formed by the chains [see Fig. 1(a)]. At intermediate densities the linkers form clusters that are, again, connected by large loops [Fig. 1(c)]. Finally, at high densities the linkers are in a dense phase, resembling a ‘‘disordered railway track’’ [Fig. 1(b)], where the chains are basically straight. We find that the crossover from the dilute regime to the dense one occurs over a narrow range of linker chemical potentials and is reminiscent of a first order phase transition. Note that this transition is similar to the isotropic-nematic transition of semiflexible chains,<sup>55</sup> where the chains become aligned at high concentrations. The driving force, however, is different; in the latter case it is the gain in translational entropy that induces the transition, whereas here the transition is induced by the interplay between the linker binding energy and the repulsive electrostatic energy between chains.

Next, by comparing the free energy of the two-chain complex with the free energy of isolated chains we show that chain pairing cannot occur in the dilute regime but only in the intermediate and dense regimes. In these regimes, the aggregation of linkers allows them to hold the two chains together against the Coulombic interchain repulsion. The results of the model compare favorably with molecular dynamics simulations of two charged chains in a mixture of monovalent and multivalent counterions at varying compositions. Here again, we find that chain pairing can only occur if the number of linkers is high enough.

### B. Comparison with bundling experiments

The aggregation of DNA (Ref. 4) and F-actin (Ref. 7) has been studied experimentally as a function of added multivalent counterions. While the length of DNA molecules (ranging from microns up to millimeters) can be orders of magnitude larger than its persistence length (50 nm), actin filaments are typically shorter than their persistence length (estimated to be a few microns). Thus, on the length scale of microns DNA can be considered to flexible while F-actin is basically rigid. Despite this important difference striking similarities were found in the experiments between these two systems.

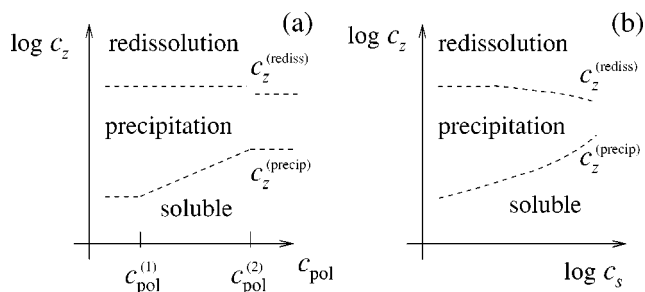


FIG. 11. Schematic view of bundling behavior as function of (a) the concentration of chains  $c_{\text{pol}}$  and (b) the concentration of salt in the solution  $c_s$ .

The main findings can be summarized as follows (see Fig. 11): In the absence of multivalent ions the chains dissolve in solution. Addition of multivalent ions induces inter-chain attraction and leads to precipitation of the chains from solution, provided that the concentration of multivalent counterions is high enough  $c_z > c_z^{(\text{precip})}$ . At low chain concentrations  $c_{\text{pol}} < c_{\text{pol}}^{(1)}$  the threshold concentration  $c_z^{(\text{precip})}$  is independent of the concentration of polymer in the solution. At higher chain concentrations  $c_{\text{pol}}^{(1)} < c_{\text{pol}} < c_{\text{pol}}^{(2)}$  the threshold concentration  $c_z^{(\text{precip})}$  depends linearly on the concentration of polymer in the solution.

In dilute polymer solutions the number of multivalent counterions in solution is not effected by the presence of chains. The solution can be therefore viewed as a reservoir of counterions with a fixed chemical potential and be treated within the *grand canonical ensemble*. Precipitation occurs when this chemical potential reaches a critical value, similar to the mechanism of chain pairing discussed earlier. In more concentrated polymer solutions all multivalent counterions are attracted to the chains and the number of adsorbed counterions per chain is determined simply by the stoichiometric ratio between the number of counterions and the number of chains in solution. Such a situation is most naturally described by the *canonical ensemble*. In analogy with the pairing mechanism, precipitation now occurs as soon as the number of adsorbed counterions per chain reaches a fixed critical value leading to a linear dependence of  $c_z^{(\text{precip})}$  on  $c_{\text{pol}}$ .

The bundled chains redissolve in the solution when the concentration of multivalent counterions becomes too high  $c_z > c_z^{(\text{rediss})}$ , where  $c_z^{(\text{rediss})}$  is of the order of 100 mM for DNA and is nearly independent of  $c_{\text{pol}}$ . This redissolution transition can be attributed to screening of electrostatic interactions by multivalent counterions.<sup>56</sup> In our pairing model  $\Gamma$  is the basic energy scale which determines how favorable the paired state is with respect to the unpaired state. Since  $\Gamma$  depends exponentially on  $\kappa$  it decreases sharply at high values of  $c_z$ ; this is consistent with the fact that  $c_z^{(\text{rediss})}$  decreases with increased salt concentration.<sup>4,7</sup> For an aqueous solution in room temperature and in the absence of salt the electrostatic screening length for  $c_z = 100$  mM is 4.4 Å for a 1:3 salt consisting of trivalent counterions and monovalent coions and 3.3 Å for a 1:4 salt. Assuming that redissolution occurs at a fixed value of the electrostatic screening length, we expect the following dependence of the redissolution concentration on the salt concentration:

$$c_z = c_z^{(0)} - 2c_s / (z^2 + 1), \quad (58)$$

where  $c_z^{(0)}$  is the limiting value of  $c_z^{(\text{rediss})}$  at low salt concentration.

The effect of monovalent salt on the bundling process is twofold. First, the monovalent counterions adsorb on the charged chains, thus competing with the multivalent ones.<sup>44,50</sup> As a result, multivalent counterions that could have become linkers are pushed into the solution. Note that since local counterion concentrations depend exponentially on their valency, the bulk concentration of monovalent salt has to be considerably larger than the concentration of multivalent counterions before the effect becomes noticeable. Second, salt enhances screening, thus leading to a decrease in the adsorption energy  $\varepsilon_0$  as well as in the electrostatic energy scale  $\Gamma$ . The combined effect is that there is an increase in the critical concentration of multivalent counterions needed to induce precipitation.<sup>4,7</sup> Experiments indicate that  $c_z^{(\text{precip})}$  and  $c_s$  might be related through a power law whose value depends on the physical properties of the chain and of the multivalent counterion.<sup>7</sup>

It should be noted that similar behavior was observed for flexible charged polymers as well.<sup>12</sup> The polymer was poly(styrene sulfonate) (PSS) whose persistence length is of the order of few angstroms. A theoretical model describing the precipitation of PSS from solution in the presence of multivalent counterions was suggested by Olvera de la Cruz *et al.*<sup>12</sup> The model attributes the attraction between polymer segments to fluctuations in the density of condensed multivalent counterions. More specifically, since the valency of the counterions is larger than the valency of the monomers the apparent charge density of the polymer chain together with its surrounding condensed counterions will be highly nonhomogeneous. Thus, monomers that are accompanied by a multivalent counterion carry an apparent charge that is opposite in sign to their bare charge and they are attracted to monomers that are not accompanied by one. The competition between this attraction and the bare electrostatic repulsion yields stability diagrams that are in reasonable agreement with PSS solubility experiments.

A different attempt to explain the solubility diagrams of more rigid chains has been suggested recently by Solis and Olvera de la Cruz.<sup>56</sup> They use a two state model consisting of a collapsed state, assumed to be an ionic glass, and an extended state, where the chains are assumed to be straight. One of their main results is that redissolution occurs when the electrostatic screening length in the collapsed state decreases below the monomer size. In an alternative model<sup>57</sup> the main mechanism driving the redissolution is overcharging of stretched charged chains by multivalent counterions. Indeed, it has been demonstrated that in the case of polyelectrolyte adsorption onto charged surfaces, charge overcompensation leads to intersurface attraction.<sup>58</sup> However, electrophoretic mobility experiments<sup>4</sup> suggest that overcompensation might not be necessary in order for aggregation to occur.

### C. Comparison with DNA denaturation

Our pairing mechanism resembles the process by which double stranded DNA (in the form of a double helix) is formed from (or decomposed into) two complementary single strands.<sup>30,31,33–35</sup> Each DNA strand is a sequence of nucleic acids, 3.4 Å apart, with four different bases: Adenine (A), Cytosine (C), Guanine (G), and Thymine (T). Each C base on one of the strands binds with a G base on the complementary strand through 3 hydrogen bonds, while A and T bind together forming 2 hydrogen bonds. The double helix is stabilized by the hydrogen bonds as well as by stacking interactions between neighboring residues, rendering its stability sequence dependent. As in our model, the hydrogen bonds compete with the bare electrostatic repulsion between the single strands, resulting from their high charge density; under normal physiological conditions each base carries one unit charge. Single strands are much more flexible than double strands but they can be also described as a semiflexible chain with a persistence length estimated to be around 40 Å.

Experiments have shown that as the temperature increases, the double helix denatures in discrete steps. At each step a section of the double helix opens up to form a loop (or bubble). The order in which DNA loops open up depends on the specific sequence: areas rich with AT pairs tend to denature at lower temperatures while those rich with GC pairs tend to denature at higher temperatures. These loops are very similar to those we predict to occur in the crossover regime of our model. Furthermore, the fact that a whole section opens up abruptly is reminiscent of the sharp jump in the binding isotherm of the linkers [e.g., Fig. 6(b)].

A few classic models of DNA denaturation have been suggested in the past.<sup>30–35,47,48</sup> These models focus mostly on the following questions: (i) Is the melting transition a true phase transition, and if it is, is it a first order or second order transition?; (ii) What is the relation between the DNA sequence and the order in which different sections of the double helix denature?

The earliest and probably the most generic model is the Poland–Scheraga model,<sup>30</sup> where each base pair is assigned a spin variable with two states: open and closed. Different statistical weights are then assigned to consecutive sequences of open pairs (loops) and closed ones (double helix). In this approach the specific properties of DNA are hidden in a few phenomenological parameters. Despite its simplicity this approach has been quite successful in relating the melting behavior of DNA to the sequence of nucleic acids.<sup>31,33</sup> The model has been also used as a starting point for studying the nature of the melting transition.<sup>30,47,48</sup> Recent studies indicate that excluded volume interactions between the nucleic acids render it a true first order phase transition.

Another approach is based on the Peyrard–Bishop model<sup>34</sup> where the degrees of freedom are the displacement of each base along the axis connecting it to the corresponding base on the adjacent strand. The model has the advantage that it allows for bond stretching and intermediate states between an open bond and a closed bond. On the other hand, the model neglects the entropy of the large loops, which play an important role due to its long ranged effect.

Our approach is complementary to the previous two. The double helix system carries many features that are common with our model. The main differences are the following. First, the linkers are not real particles whose total number is conserved but rather bonds that can be either open or closed. A similar distinction between the Ising model and the standard lattice gas model can be bridged using a mathematical mapping between the partition functions of the two models. Second, since bonds can be formed between every base pair the linkers are not free to move continuously along the chains but are restricted to a discrete set of fixed positions located 3.4 Å apart. We note that our approach can be generalized to include sequence-specific bond energies. The main advantage of our model over previous approaches is that we explicitly include electrostatic interactions, which are known to play an important role in such systems, and chain bending rigidity as well. Our approach is therefore a natural one for studying electrostatic denaturation of DNA. It is also well-suited for studying tension-induced denaturation of DNA with or without binding proteins.<sup>59</sup>

### D. Final remarks

The point of view adopted here, of treating multivalent ions or binding proteins as generalized linkers, is useful because it provides a unifying framework for treating the aggregation of charged semiflexible chains. Within this framework we can understand why the phenomenon of bundling is strikingly similar for all systems of charged semiflexible chains. For example, bundling occurs when the quality of solvent is reduced; this gives rise to effective attractions. A model containing this attraction can be mapped onto a model containing linkers, just as hydrogen bonds can be mapped onto linkers as described for DNA denaturation above. Bundling also occurs when neutral polymers such as PEG are added, due to depletion interactions [as in  $\psi$ -condensation of DNA (Ref. 60)]. The depletion attractions become attractive at short distances when the PEG concentration is high enough, much as in the case of added linkers. Thus, our conclusions apply very generally to systems with charged semiflexible chains in solution, not only in the presence of explicit condensing agents such as multivalent ions or bundling or crosslinking proteins, but also when short-ranged attractive interactions of various sources are present.

Our approach appears limited because we have considered only two chains. What are the consequences of linkers in many-chain systems? Here we argue that the mechanism for a phase transition between a dilute linker phase and a dense linker phase transcends the two-chain model. We have found that the bare electrostatic repulsion between the charged chains leads to an effective attraction between linkers along the chains that results in a rounded phase transition in the two-chain case. In a many-chain system, there is still an electrostatic cost for every junction. If more than one linker clusters at a junction, the number of junctions decreases and the energy per junction also decreases. This mechanism for an effective attraction between linkers should apply in the many-chain system as well as the two-chain system. We therefore expect that in a many-chain system, there is a true phase transition from a dilute linker phase to a dense linker phase. In the dilute linker phase, the chains

cross at large angles; this is a network. In the dense linker phase, the chains are nearly parallel and densely packed; this is a bundle. The existence of a phase transition between networks and bundles may be relevant to the cytosol of cells such as blood platelets. Micrographs of the cytosol show that bundles of F-actin can exist in close proximity to and actually merge into networks of F-actin.<sup>61</sup> This implies that the self-assembled structure is highly sensitive to gradients in the concentration of various bundling and crosslinking proteins. We know that high sensitivity to concentration can be found in the vicinity of a phase transition. We therefore suggest that this might not be a coincidence; if the system is tuned to be near a phase transition, small amounts of specific proteins can be used to drive the system from one phase to another.

### ACKNOWLEDGMENTS

We would like to thank A. Ben-Shaul, C. Marques, H. Schiessel, J.-L. Sikorav, and J. Widom for valuable discussions. Support from NSF Grant No. DMR-9708646 and Israel-U.S. BSF Grant No. 97-00205 is gratefully acknowledged.

### APPENDIX: ANALYTIC RESULTS

#### 1. The dilute regime

At low linker densities  $\rho \ll 1/l^*$  the average interlinker separation is large and the main contribution to the partition function comes from the long range ( $l \geq l^*$ ) part of the potential. The potential can then be approximated by

$$v_{\text{long}}(l) \approx \frac{\alpha l_p}{l} + c \ln(l/l_p). \quad (\text{A1})$$

For  $c = 3/2$  the partition function can be calculated exactly<sup>62</sup> yielding

$$Z_1 = \sqrt{\frac{\pi \lambda_T}{\alpha l_p}} e^{-\sqrt{4\alpha l_p P}}. \quad (\text{A2})$$

In the thermodynamic limit  $N, L \rightarrow \infty$  the Gibbs potential becomes

$$G(N, P, T) = N \left[ \sqrt{\frac{\pi \lambda_T}{\alpha l_p}} + \sqrt{4\alpha l_p P} \right]. \quad (\text{A3})$$

Extracting  $L$  as function of  $P$  [using and inverting Eq. (31)] gives the following equation of state:

$$P(\rho, T) = \alpha l_p \rho^2. \quad (\text{A4})$$

The dependence of the pressure on the density is typical of systems with repulsive interactions where  $l_p$  plays the role of a one-dimensional second virial coefficient (up to numerical prefactors).

The free energy density and chemical potential are

$$f_{\text{tot}}(\rho, T) = \alpha l_p \rho^2 + \rho \ln \left( \sqrt{\frac{\alpha \lambda_T}{\pi l_p}} \right) + (\Gamma - 2\varepsilon_0) \rho, \quad (\text{A5})$$

$$\mu_{\text{tot}}(\rho, T) = 2\alpha l_p \rho + \ln \left( \sqrt{\frac{\alpha \lambda_T}{\pi l_p}} \right) + \Gamma - 2\varepsilon_0. \quad (\text{A6})$$

The first term represents the chain mediated interlinker repulsion while the last term is just a constant shift in the chemical potential of the linkers. Note the cancellation of the logarithmic dependencies on linker density of the translational entropy and the loop entropy.

The compressibility and the fluctuations in the linker separations are

$$\rho \kappa_T = \frac{1}{2\alpha l_p \rho}, \quad (\text{A7})$$

$$\rho \Delta l = \frac{1}{\sqrt{2\alpha l_p \rho}}. \quad (\text{A8})$$

#### 2. The dense regime: Neutral linkers

At small separations ( $l \leq l^*$ ) the chain-mediated interlinker interaction depends linearly on  $l$ ,

$$v_{\text{short}}(l) \approx -\Gamma(1 - l/l_0). \quad (\text{A9})$$

With only hard core interactions the partition function becomes

$$Z_1 = \frac{e^{\Gamma - (P + P_0)b}}{\lambda_T(P + P_0)}, \quad (\text{A10})$$

where  $P_0 \equiv \Gamma/l_0$ . In the thermodynamic limit the Gibbs potential is

$$G(N, P, T) = N[\ln \lambda_T(P + P_0) + (P + P_0)b - \Gamma], \quad (\text{A11})$$

and the equation of state

$$(P + P_0)(L - Nb) = N. \quad (\text{A12})$$

Note the resemblance to the van der Waals equation of state. The attractive part of the potential reduces the pressure by an amount equal to  $P_0$ , while the volume of the system is reduced by the excluded volume  $Nb$ .

The free energy and the chemical potential are

$$f_{\text{tot}}(\rho, T) = \rho \left[ \ln \left( \frac{\lambda_T \rho}{1 - \rho b} \right) - 1 \right] + P_0 - 2\varepsilon_0 \rho, \quad (\text{A13})$$

$$\mu_{\text{tot}}(\rho, T) = \ln \left( \frac{\lambda_T \rho}{1 - \rho b} \right) + \frac{\rho b}{1 - \rho b} - 2\varepsilon_0, \quad (\text{A14})$$

while the isothermal compressibility and fluctuations in the linker separations are

$$\rho \kappa_T = (1 - \rho b)^2, \quad (\text{A15})$$

$$\rho \Delta l = 1 - \rho b. \quad (\text{A16})$$

Note that the energy gain  $-\Gamma$  per linker [Eqs. (A13), (A14)] cancels the electrostatic cost of forming a junction [Eqs. (39), (41)].

#### 3. The dense regimes: Charged linkers ( $z > 0$ )

If the linkers are charged the interlinker potential includes an additional repulsive term at short distances. Neglecting the effect of screening on the bare interlinker potential and the hard core interaction, the potential now becomes

$$v(l) = -\Gamma(1 - l/l_0) + z^2 l_B/l, \quad (\text{A17})$$

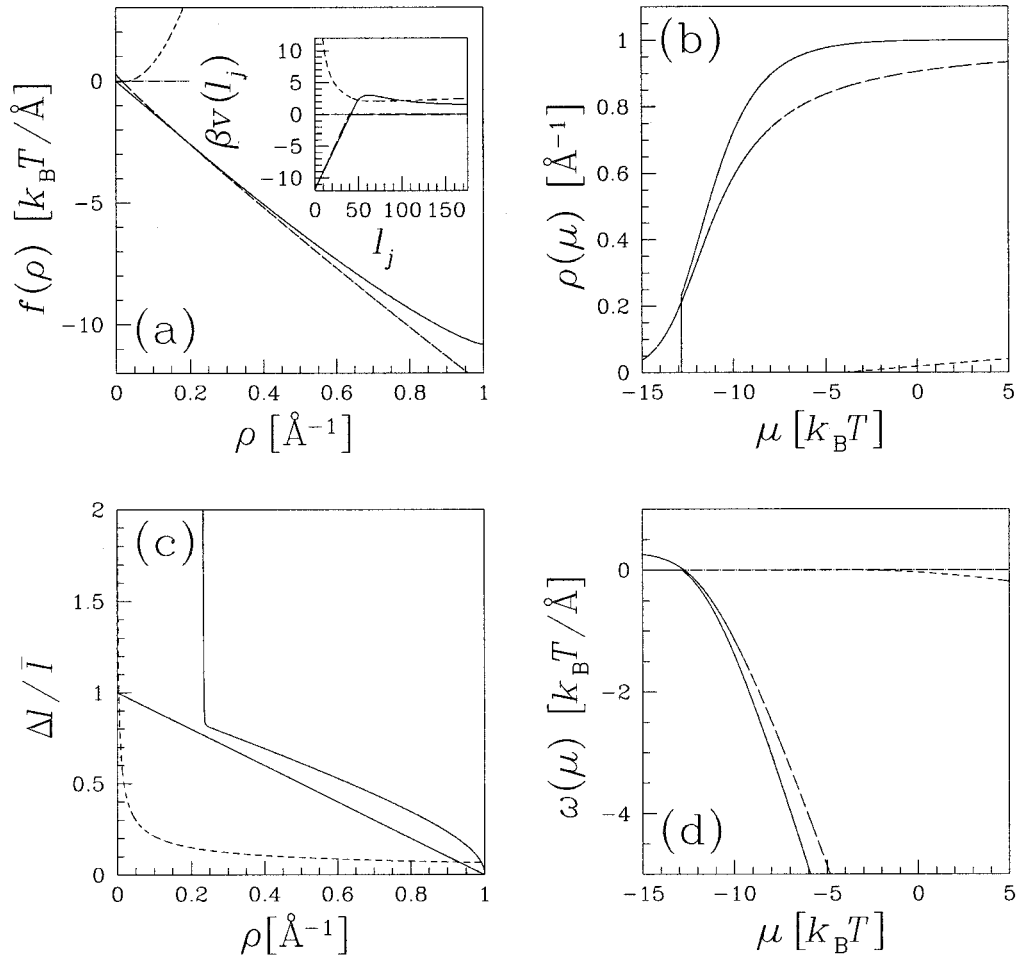


FIG. 12. Comparison of the numerical calculation with the analytic approximations for the data described in Fig. 6 (solid curve). The solid curves are the numerical results while the short and long dashed curves correspond to the dilute regime and the dense regime, respectively. The values of the physical quantities used in the calculation are  $\kappa^{-1}=10$  Å,  $l_B=7$  Å,  $\xi=4$ ,  $d=25$  Å,  $l_p=50$  Å,  $z=0$ ,  $b=1$  Å, and  $\lambda_T=1$  Å.

where  $P_0$  was defined above. The partition function is

$$Z_1 = \frac{e^\Gamma}{\lambda_T} \sqrt{\frac{4z^2 l_B}{P+P_0}} K_1(\sqrt{4z^2 l_B(P+P_0)}), \quad (\text{A18})$$

and the Gibbs free energy

$$G(N, P, T) = N \left[ \ln \lambda_T \left( \frac{P+P_0}{4z^2 l_B} \right) - \ln K_1(\sqrt{4z^2 l_B(P+P_0)}) - \Gamma \right]. \quad (\text{A19})$$

Using the asymptotic behavior of the Bessel function for large arguments (valid in the high pressure/high density regime) we obtain the following equation of state:

$$P + P_0 \approx z^2 l_B \rho^2, \quad z^2 l_B \rho \gg 1. \quad (\text{A20})$$

The free energy density, the chemical potential and the compressibility are

$$f(\rho, T) = \rho \ln \lambda_T \rho + z^2 l_B \rho^2 + \frac{1}{2} \rho \ln[z^2 l_B \rho / \pi] + P_0 - \Gamma \rho, \quad (\text{A21})$$

$$\mu(\rho, T) = \ln \lambda_T \rho + 2z^2 l_B \rho + \frac{1}{2} \ln[z^2 l_B \rho / \pi] - \Gamma, \quad (\text{A22})$$

$$\rho \kappa_T = \frac{1}{2z^2 l_B \rho}. \quad (\text{A23})$$

#### 4. Comparison with numerical results

The analytic expressions derived above can be compared now with the numerical calculations. We consider here neutral linkers with only hard core interactions (Fig. 12). The solid curves are the numerical data from Fig. 6, to be compared with the short dashed curves (dilute regime) and the long dashed curves (dense regime). The qualitative features are well described by the analytical expressions although some quantitative features are different.

Consider first the situation where the linker density  $\rho$  is fixed [Fig. 12(a)]. In the dilute regime the minimum of the free energy is at a low value of the linker density  $\rho_{\text{dilute}}^* \ll 1/b$  and the value of the free energy at the minimum is close to zero. On the other hand, in the dense regime the minimum is close to the close packing density  $\rho \rightarrow 1/b$  and has a strong negative value which is of the order of  $-\Gamma$ . At the crossover from the dilute regime to the dense one both the chemical potentials and the pressures in the two phases are equal. The result is two implicit equations for the densi-

ties  $\rho_{\text{dilute}}$ ,  $\rho_{\text{dense}}$  in the two regimes at the crossover,

$$\mu_{\text{tot}}^{(\text{dilute})}(\rho^{(\text{dilute})}) = \mu_{\text{tot}}^{(\text{dense})}(\rho^{(\text{dense})}), \quad (\text{A24})$$

$$P^{(\text{dilute})}(\rho^{(\text{dilute})}) = P^{(\text{dense})}(\rho^{(\text{dense})}), \quad (\text{A25})$$

where  $\mu_{\text{tot}}^{(\text{dilute})}$  and  $\mu_{\text{tot}}^{(\text{dense})}$  are given by Eqs. (39), (A6), (A14) while  $P^{(\text{dilute})}$  and  $P^{(\text{dense})}$  are given by Eqs. (A4), (A12).

Since  $\rho^{(\text{dilute})} \ll \rho^{(\text{dense})} \approx 1/b$  one can extract from the pressure equality [Eq. (A25)] a lower bound on the density in the dense regime,

$$\rho^{(\text{dense})} \geq \frac{P_0}{1 + P_0 b}, \quad (\text{A26})$$

and an approximate crossover chemical potential

$$\mu^* \geq \ln \lambda_T \rho - \Gamma, \quad (\text{A27})$$

$$\mu_{\text{tot}}^* \geq \ln \lambda_T \rho - 2\varepsilon_0. \quad (\text{A28})$$

For the parameters of Fig. 12 we obtain  $\rho^{(\text{dense})} \geq 0.23$  and  $\mu^* \geq -13.3$  which are in reasonable agreement with the numerical results.

Below the crossover point the density is low and can be approximated by the short dashed curve while above that point it approaches the close packing density  $1/b$  as is described by the long dashed curve.

The crossover is accompanied by a strong increase in the fluctuations of the interlinker distance [solid curve; Fig. 12(c)]. Since the analytic expressions are only valid well within each regime and not at the crossover, the peak in the fluctuations  $\Delta l/\bar{l}$  is not reproduced. In addition, the fluctuations in the dense regime are not well reproduced in the analytic approximation. The numeric results indicate that  $\Delta l/\bar{l} \approx (1 - \rho b)^{2/3}$  instead of the linear dependence predicted by Eq. (A16).

In a fixed chemical potential ensemble the crossover from the dilute regime to the dense regime is determined by the grand canonical potential  $\omega(\mu)$  depicted in Fig. 12(d). Below the crossover point  $\mu < \mu^*$  the potential of the dilute phase is lower than that of the dense phase. At  $\mu = \mu^*$  the potentials are equal and then at  $\mu > \mu^*$  the grand canonical potential is lower in the dense phase. Note that, since  $\omega = -P$ , equating the grand canonical potentials is equivalent to equating the linker pressures.

- <sup>11</sup>At the other extreme are charged linear polymers such as poly(styrene sulfonate) (PSS) that are so flexible that they condense into globular aggregates in the presence of multivalent counterions (Ref. 12).
- <sup>12</sup>M. Olvera de la Cruz, L. Belloni, M. Delsanti, J. P. Dalbiez, O. Spalla, and M. Drifford, *J. Chem. Phys.* **103**, 5781 (1995). Even for flexible chains one might expect a loose network at low enough multivalent counterion concentrations.
- <sup>13</sup>D. C. Rau and V. A. Parsegian, *Biophys. J.* **260**, 260 (1992).
- <sup>14</sup>F. Oosawa, *Polyelectrolytes* (Marcel Dekker, New York, 1971).
- <sup>15</sup>J. Ray and G. S. Manning, *Langmuir* **10**, 2450 (1994).
- <sup>16</sup>A. P. Lyubartsev and L. Nordenskiöld, *J. Phys. Chem.* **99**, 10373 (1995).
- <sup>17</sup>J. L. Barrat and J. F. Joanny, *Adv. Chem. Phys.* **94**, 1 (1996).
- <sup>18</sup>N. Grønbech-Jensen, R. J. Mashl, R. F. Bruinsma, and W. M. Gelbart, *Phys. Rev. Lett.* **78**, 2477 (1997).
- <sup>19</sup>B.-Y. Ha and A. J. Liu, *Phys. Rev. Lett.* **79**, 1289 (1997); **81**, 1011 (1998).
- <sup>20</sup>B.-Y. Ha and A. J. Liu, *Phys. Rev. E* **58**, 6281 (1998); **60**, 803 (1999).
- <sup>21</sup>M. Stevens, *Phys. Rev. Lett.* **82**, 101 (1999); *Biophys. J.* **80**, 130 (2001).
- <sup>22</sup>B. I. Shklovskii, *Phys. Rev. Lett.* **82**, 3268 (1999).
- <sup>23</sup>F. J. Solis and M. Olvera de la Cruz, *Phys. Rev. E* **60**, 4496 (1999).
- <sup>24</sup>R. Kjellander, T. Åkesson, B. Jönsson, and S. Marčelja, *J. Chem. Phys.* **97**, 1424 (1992); P. Kékicheff, S. Marčelja, T. J. Senden, and V. E. Shubin, *ibid.* **99**, 6098 (1993).
- <sup>25</sup>I. Rouzina and V. A. Bloomfield, *J. Phys. Chem.* **100**, 9977 (1996).
- <sup>26</sup>A. W. C. Lau, D. Levine, and P. Pincus, *Phys. Rev. Lett.* **84**, 4116 (2000); A. W. C. Lau, P. Pincus, D. Levine, and H. A. Fertig, *Phys. Rev. E* **6305**, 1604 (2001).
- <sup>27</sup>P. A. Pincus and S. A. Safran, *Europhys. Lett.* **42**, 103 (1998).
- <sup>28</sup>I. Borukhov, R. F. Bruinsma, W. M. Gelbart, and A. J. Liu, *Phys. Rev. Lett.* **86**, 2182 (2001).
- <sup>29</sup>I. Borukhov and R. F. Bruinsma, *Phys. Rev. Lett.* **87**, 158 101 (2001).
- <sup>30</sup>D. Poland and H. A. Scheraga, *Theory of Helix-Coil Transitions in Biopolymers* (Academic, New York, 1970).
- <sup>31</sup>M. Ya, *Phys. Rev. A* **20**, 1671 (1979).
- <sup>32</sup>J. H. Shibata and J. M. Schurr, *Biopolymers* **20**, 525 (1981).
- <sup>33</sup>R. M. Wartell and A. S. Benight, *Phys. Rep.* **126**, 67 (1985).
- <sup>34</sup>M. Peyrard and A. R. Bishop, *Phys. Rev. Lett.* **62**, 2755 (1989).
- <sup>35</sup>A. Yu. Grosberg and A. R. Khokhlov, *Statistical Physics of Macromolecules* (AIP, New York, 1994).
- <sup>36</sup>Intrachain interactions will not be treated explicitly here since their main effect is to renormalize the chain rigidity (see, e.g., Refs. 37–42).
- <sup>37</sup>T. Odijk, *J. Polym. Sci., Polym. Phys. Ed.* **15**, 477 (1977); J. Skolnick and M. Fixman, *Macromolecules* **10**, 944 (1977).
- <sup>38</sup>I. Rouzina and V. A. Bloomfield, *Biophys. J.* **74**, 3152 (1998).
- <sup>39</sup>R. Golestanian, M. Kardar, and T. B. Liverpool, *Phys. Rev. Lett.* **82**, 4456 (1999).
- <sup>40</sup>P. L. Hansen, D. Svehšek, A. Parsegian, and R. Podgornik, *Phys. Rev. E* **60**, 1956 (1999).
- <sup>41</sup>H. Diamant and D. Andelman, *Phys. Rev. E* **61**, 6740 (2000).
- <sup>42</sup>R. Zandi, J. Rudnick, and R. Golestanian, *Europhys. Lett.* (submitted); E-print: cond-mat/0103207.
- <sup>43</sup>S. L. Brenner and V. A. Parsegian, *Biophys. J.* **14**, 327 (1974).
- <sup>44</sup>G. S. Manning, *Q. Rev. Biophys.* **11**, 2 (1978).
- <sup>45</sup>C. Bustamente, J. F. Marko, E. D. Siggia, and S. Smith, *Science* **265**, 1599 (1994).
- <sup>46</sup>K.-C. Lee, I. Borukhov, W. M. Gelbart, A. J. Liu, and M. J. Stevens (unpublished).
- <sup>47</sup>M. E. Fisher, *J. Chem. Phys.* **45**, 1469 (1966).
- <sup>48</sup>M. S. Causo, B. Coluzzi, and P. Grassberger, *Phys. Rev. E* **62**, 3958 (2000); Y. Kafri, D. Mukamel, and L. Peliti, *Phys. Rev. Lett.* **85**, 4988 (2000); T. Garel, C. Monthus, and H. Orland, *Europhys. Lett.* **55**, 132 (2001); E. Carlon, E. Orlandini, and A. L. Stella, *Phys. Rev. Lett.* **88**, 198101 (2002).
- <sup>49</sup>See, e.g., E. H. Lieb and D. C. Mattis, *Mathematical Physics in One Dimension* (Academic, New York, 1966), and references therein.
- <sup>50</sup>I. Rouzina and V. A. Bloomfield, *J. Phys. Chem.* **100**, 4292 (1996); *Biophys. Chem.* **64**, 139 (1997).
- <sup>51</sup>R. W. Hockney and J. W. Eastwood, *Computer Simulations Using Particles* (Adam Hilger, Bristol, 1988).
- <sup>52</sup>VMD was developed by the Theoretical Biophysics Group in the Beckman Institute for Advanced Science and Technology at the University of Illinois at Urbana-Champaign. See W. Humphrey, A. Dalke, and K. Schulten, *J. Mol. Graphics* **14**, 33 (1996).
- <sup>53</sup>See, e.g., J. M. Thijssen, *Computational Physics* (Cambridge University

<sup>1</sup>L. C. Gosule and J. A. Schellman, *Nature (London)* **259**, 333 (1976).

<sup>2</sup>J. Widom and R. L. Baldwin, *J. Mol. Biol.* **144**, 431 (1980); *Biopolymers* **22**, 1595 (1983).

<sup>3</sup>V. A. Bloomfield, *Biopolymers* **31**, 1471 (1991); H. Deng and V. A. Bloomfield, *Biophys. J.* **77**, 1556 (1999).

<sup>4</sup>J. Pelta, F. Livolant, and J.-L. Sikorav, *J. Biol. Chem.* **271**, 5656 (1996); E. Raspaud, M. Olvera de la Cruz, J.-L. Sikorav, and F. Livolant, *Biophys. J.* **74**, 381 (1998); E. Raspaud, I. Chaperon, A. Leforestier, and F. Livolant, *ibid.* **77**, 1547 (1999).

<sup>5</sup>M. Kawamura and K. Maruyama, *J. Biochem. (Tokyo)* **68**, 899 (1970).

<sup>6</sup>T. D. Pollard and J. A. Cooper, *Annu. Rev. Biochem.* **55**, 987 (1986).

<sup>7</sup>J. X. Tang and P. A. Janmey, *J. Biol. Chem.* **271**, 8556 (1996); J. X. Tang, Sh. Wong, Ph. T. Tran, and P. A. Janmey, *Ber. Bunsenges. Phys. Chem.* **100**, 796 (1996).

<sup>8</sup>Z. Shao, D. Shi, and A. V. Somlyo, *Biophys. J.* **78**, 950 (2000).

<sup>9</sup>C. Safinya and G. Wong (private communication).

<sup>10</sup>Y. Cohen and E. Cohen, *Macromolecules* **28**, 3631 (1995).

- Press, Cambridge, 1999); D. Frenkel and B. Smit, *Understanding Molecular Simulations* (Academic, San Diego, 1996).
- <sup>54</sup>B.-Y. Ha and A. J. Liu, *Europhys. Lett.* **46**, 624 (1999).
- <sup>55</sup>For rod lengths exceeding the persistence length (of order 10  $\mu\text{m}$  for Actin) one must replace  $L$  with the persistence length. See, e.g., A. R. Khokhlov and A. N. Semenov, *Physica A* **108**, 546 (1981); **112**, 605 (1982); Z. Y. Chen, *Macromolecules* **26**, 3419 (1993); J. X. Tang and S. Fraden, *Liq. Cryst.* **19**, 459 (1995).
- <sup>56</sup>F. J. Solis and M. Olvera de la Cruz, *J. Chem. Phys.* **112**, 2030 (2000); *Eur. Phys. J. E* **4**, 143 (2001).
- <sup>57</sup>T. T. Nguyen, I. Rouzina, and B. I. Shklovskii, *J. Chem. Phys.* **112**, 2562 (2000).
- <sup>58</sup>I. Borukhov, D. Andelman, and H. Orland, *J. Phys. Chem. B* **103**, 5042 (1999).
- <sup>59</sup>M. C. Williams, J. R. Wenner, I. Rouzina, and V. A. Bloomfield, *Biophys. J.* **80**, 874 (2001); **80**, 1932 (2001); M. C. Williams, I. Rouzina, J. R. Wenner, R. J. Gorelick, K. Musier-Forsyth, and V. A. Bloomfield, *Proc. Natl. Acad. Sci. U.S.A.* **98**, 6121 (2001).
- <sup>60</sup>A. Yu. Grosberg, I. Ya. Erukhimovitch, and E. I. Shakhnovitch, *Biopolymers* **21**, 2413 (1982); R. de Vries, *Biophys. J.* **80**, 1186 (2001).
- <sup>61</sup>H. Lodish *et al.*, *Molecular Cell Biology*, 4th ed. (Freeman, New York, 2000).
- <sup>62</sup>H. Schiessel, J. Rudnick, R. F. Bruinsma, and W. M. Gelbart, *Europhys. Lett.* **51**, 237 (2000).